LA-MC-ICP-MS U-Pb dating of low-U garnets reveals multiple episodes of skarn formation in the volcanic-hosted iron mineralization system, Awulale belt, Central Asia

Shuang Yan[1,2], Renjie Zhou[2], He-Cai Niu[1,†], Yue-xing Feng[2], Ai Duc Nguyen[2], Zhen-hua Zhao[1], Wu-Bin Yang[1], Qian Dong[3], and Jian-xin Zhao[2,4,†]

[1]*CAS Key Laboratory of Mineralogy and Metallogeny/Guangdong Provincial Key Laboratory of Mineral Physics and Materials, Guangzhou Institute of Geochemistry, Chinese Academy of Sciences (CAS), Guangzhou 510640, China*
[2]*School of Earth and Environmental Sciences, The University of Queensland, Brisbane, QLD 4072, Australia*
[3]*Beijing Research Institute of Uranium Geology, Beijing 100029, China*
[4]*Beijing SHRIMP Center, Institute of Geology, Chinese Academy of Geological Sciences, Beijing 100037, China*

ABSTRACT

Volcanic-hosted iron deposits of the eastern Awulale metallogenetic belt in Central Asia possess a reserve of over 1.2 billion tons of iron ores and constitute one of the most important basements for high-grade iron resources in China. Skarns are widespread in these deposits and closely associated with iron mineralization. The ages of these skarns are unclear, and their genesis remains debated, preventing further investigation into their metallogenic processes. We focused on garnets in nine ore-bearing skarns from three large-scale iron deposits (Chagangnuoer, Dunde, and Beizhan) in the eastern Awulale belt. U-Pb dating was conducted on these garnets using our in-house reference material, the Taochong garnet (TC-13, Pb-Pb isochron age: 126.2 ± 2.3 Ma, initial $^{207}Pb/^{206}Pb$ ratio: 0.845 ± 0.022). Laser-ablation–multicollector–inductively coupled plasma–mass spectrometry (LA-MC-ICP-MS) was employed in the garnet U-Pb dating, and high-precision U-Pb ages (0.3%–1.6%) were obtained, highlighting the advantages of LA-MC-ICP-MS in dating low-U minerals. The garnet U-Pb ages of the nine skarn samples fall into three groups, i.e., 329.0 ± 5.1–326 ± 3.3 Ma (two samples), 316.3 ± 2.9–311.2 ± 2.4 Ma (six samples), and 295.6 ± 1.0 Ma (one sample), implying three episodes of skarn alteration in the volcanic-hosted iron mineralization system. The first and second episodes of skarns formed as a result of contact metasomatism between coeval volcanic rocks and limestone, and they have economically important iron mineralization. The third was likely caused by a local postcollision granitic intrusion, but its metallogenic potential deserves further assessment.

INTRODUCTION

Garnet is a commonly used mineral in geochronology (Baxter and Scherer, 2013; Smit et al., 2013) and can be dated using multiple approaches, such as the Sm-Nd isochron, Lu-Hf isochron, Pb-Pb isochron, and isotope dilution–thermal ionization mass spectrometry (ID-TIMS) U-Pb methods (Cheng et al., 2018; Jung and Mezger, 2003; Salnikova et al., 2018; Scherer et al., 2000; Smit et al., 2013). These geochronometers act as powerful tools to obtain garnet ages, but they are very time-consuming and costly. In situ U-Pb dating with laser ablation has recently become available to date garnets in skarn and syenite (Deng et al., 2017; Gevedon et al., 2018; Seman et al., 2017; Wafforn et al., 2018) and in carbonatite and alkaline complexes (Yang et al., 2018). This method has greatly facilitated garnet U-Pb geochronology due to its high spatial resolution and rapid data acquisition. Though these datable garnets contain some common lead, precise U-Pb isotopic ages (precision <3%) can be obtained provided the U-Pb isotopic compositions from the same sample spread along a mixing line between common Pb and radiogenic Pb components (Chew et al., 2011, 2014; Roberts et al., 2017; Simonetti et al., 2006). A challenge lies in samples with sub–part per million uranium (U) contents; their age determination requires instruments with a higher sensitivity.

With in situ analytical methods, trace elements at concentrations measurable by laser-ablation–inductively coupled plasma–mass spectrometry (LA-ICP-MS) can also be obtained from garnets (Gaspar et al., 2008; Smith et al., 2004). Among them, rare earth elements (REEs) and U stand out as useful geochemical tracers in both magmatic and hydrothermal systems (Jamtveit and Hervig, 1994; Morgan, 1990; Park et al., 2017; Whitney and Olmsted, 1998). REE behaviors in garnet are primarily controlled by their regular decrease in ionic radii, but these values may become highly variable in skarn systems due to their dependence on protoliths, the position relative to fluid sources (water/rock ratios), and major-element concentrations (Gaspar et al., 2008; Jamtveit and Hervig, 1994; Smith et al., 2004; Whitney and Olmsted, 1998). The incorporation of U into a grandite lattice is dominated by substitution at the Ca site, and U^{4+} is more likely to substitute into grandite than U^{6+} on the basis of ionic radius (Shannon, 1976; Smith et al., 2004). Moreover, the U content of garnets usually positively correlates with those of total REEs, suggesting that processes controlling REE behaviors may also control the uptake of U in grandite-forming fluids (Smith et al., 2004). A few researchers have successfully deciphered the geological history of skarns by investigating REE and U geochemistry in different types of skarn deposits (Park et al., 2017; Whitney and Olmsted, 1998; Xiao et al., 2018). When combined with geochronological data of skarn garnets, REE and U geochemistry of garnets can be an attractive tool with which to constrain the origins and properties of hydrothermal fluids in skarn systems.

†Corresponding authors: niuhc@gig.ac.cn (He-Cai Niu); j.zhao@uq.edu.au (Jian-xin Zhao).

The Awulale metallogenetic belt in the western Tianshan, Central Asia, is a well-known region for hosting plentiful volcanic-hosted iron deposits (Hou et al., 2014). Skarns are pervasive in these deposits and display a close relationship with iron orebodies, both spatially and temporally (Duan et al., 2014; Hong et al., 2012; Yan et al., 2018). However, skarn genesis in these volcanic-hosted iron deposits has not been well understood due to the lack of geochronological data and the complex spatial relationships between skarns and wall rocks. Various models have been proposed for skarn genesis and iron mineralization of these deposits, including pluton-related contact metasomatism (Duan et al., 2014), basaltic magma and limestone reaction (Sun et al., 2015), and volcanic hydrothermal metasomatism (Yan et al., 2018). In all these models, skarns are thought to form as a result of metasomatism between magmatic and carbonate rocks, whereby magmatic rocks in ore districts were causative igneous rocks and the limestone strata provided the carbonate component for the skarns. However, it is difficult to test the linkages between individual skarn deposits and magmatism due to the presence of multiple magmatic rocks in the volcanic-hosted system. Constraints on the timing of skarn formation become a critical piece of evidence in testing models that link the formation of skarns and skarn-hosted mineral deposits with magmatic rocks. Skarns generally develop coevally with, or slightly later than their causative igneous rocks, and their chemical compositions, to some extent, also originate from their precursors (Grant, 1986; Jansson and Allen, 2013; Meinert, 1992; Meinert et al., 2005). Garnets form during the early stage of skarn alteration and are ideal proxies with which to investigate the timing and geochemical properties of skarns. Geochronological and geochemical data from skarn garnets may provide significant information for pinpointing potential source rocks. Therefore, we investigated in situ U-Pb ages and REE geochemistry of skarn garnets from three volcanic-hosted iron deposits (Chagangnuoer, Dunde, and Beizhan) to reveal skarn genesis and provide insights into their metallogenesis. Notably, some skarn garnets only contained sub–part per million U contents. In this study, we demonstrated that high-precision garnet U-Pb ages can be obtained using multicollector (MC) LA-ICP-MS instruments.

BACKGROUND AND SAMPLES

Regional Geology

The Chinese western Tianshan of the Central Asian orogenic belt (Fig. 1A) is located between the Junggar plate to the north and the Tarim plate to the south and can be subdivided into three parts, the North Tianshan, the Yili–Central Tianshan, and the South Tianshan (Allen et al., 1993; Gao et al., 2009). The Awulale orogenic belt lies in the eastern part of the Yili block and tapers to a point where the North Tianshan fault and the north Nalati fault converge (Fig. 1B). It has a Mesoproterozoic metamorphic crystalline basement, predominately composed of marble, biotite-plagioclase gneiss, and hornblende-plagioclase gneiss (Feng et al., 2010), which is covered by series of carbonate-volcanic, marine volcanic and volcaniclastic, terrigenous clastic-carbonate, and terrigenous clastic rocks formed from the Silurian to the Jurassic (Fig. 1C; Liu et al., 2014; Wang et al., 2014).

The Awulale orogenic belt hosts a major polymetallic metallogenetic belt in western Tianshan, the Awulale metallogenetic belt (Fig. 1C; Hou et al., 2014; Zhang et al., 2014). From west to east in the eastern Awulale metallogenetic belt, five large-to-medium volcanic-hosted iron (Fe) deposits, namely, the Wuling Fe deposit, Chagangnuoer Fe deposit, Zhibo Fe deposit, Dunde Fe-Zn deposit, and Beizhan Fe deposit, have been explored, and are all hosted in volcanic/volcaniclastic rocks of the late Carboniferous Dahalajunshan Formation (Fig. 1C). Remote-sensing satellite imagery indicates that the five deposits are distributed around the same caldera crater (Feng et al., 2010). The Zhibo deposit is located in the center of the caldera and is characterized by magmatic mineralization with abundant magmatic magnetite ores, widespread K-feldspar alteration, and diopside alteration (Feng et al., 2010; Zhang et al., 2012a). The Wuling and Chagangnuoer deposits lie on the margin of the caldera crater, and the latter one has both magmatic and hydrothermal mineralization and widespread skarn (Feng et al., 2010; Wang et al., 2011). The Dunde and Beizhan deposits are situated along radial fractures distal from the caldera center and are characterized by magmatic hydrothermal mineralization and pervasive skarn alteration (Duan et al., 2014; Ge, 2013; Yan et al., 2018). During volcanic processes, magmatic activities weaken and hydrothermal activities strengthen from the proximal to the distal zones, correspondingly resulting in different mineralization types for deposits distributed from the caldera crater outward. The five deposits are probably genetically related, and the volcanic magmatism and resultant hydrothermal activity may have triggered regional iron mineralization of the eastern Awulale metallogenetic belt. In this study, we only focused on the Chagangnuoer, Dunde, and Beizhan deposits, where garnet-bearing skarns are widely exposed.

Deposit Geology and Samples

The Chagangnuoer Fe deposit is a large Fe deposit with an iron reserve of over 200 Mt at 35 wt% (Fig. 2A). Iron orebodies and skarn zones are hosted in the second subformation of the Dahalajunshan Formation, which is composed of ferrobasalt, andesitic tuff, trachyandesite, dacite, rhyolitic tuff, and a small amount of thin-bedded limestone. Zircon U-Pb ages obtained for the ferrobasalt, dacite, and trachyandesite are 314 ± 8 Ma (Li et al., 2015), 313 ± 6 Ma (unpublished age of our research team), and 328.7 ± 2.7 Ma (Feng et al., 2010), respectively. In the Fe I ore district, a garnet skarn zone, magnetite orebody, actinolite-epidote skarn zone, and marble zone are exposed from east to west. Sm-Nd isochron ages of garnet and skarn are 316.8 ± 6.7 Ma (Hong et al., 2012) and 313 ± 7 Ma (Zhang et al., 2015), respectively. Three ore-bearing skarns (CG2801, 11CG11-2, and 11CG15-20) were sampled at Chagangnuoer. Among them, sample CG2801 is a drill-core sample, while the other two were collected from outcrops. These skarns are composed predominantly of garnet and magnetite with lesser epidote and actinolite (Fig. 3). Garnet grains are reddish brown in color (Fig. 3), automorphic, and coarse in size (0.5–1 cm; Fig. 4). In sample CG2801, garnet crystals include magnetite, while in samples 11CG11-2 and 11CG15-20, garnet and magnetite cement each other, indicating coprecipitation. The spatial relationship of garnet and magnetite in the samples reveals their precipitation sequence, and thus garnet ages can also constrain the timing of magnetite precipitation.

The Dunde Fe-Zn deposit is a large Fe deposit with a proven reserve of 185 Mt of iron ore at 35.06% and 1.49 Mt of Zn ore at 1.26% (Fig. 2B; Duan et al., 2014). Its orebodies are hosted by volcanic rocks of dacite, rhyolite, basaltic tuff, and andesitic tuff of the late Carboniferous Dahalajunshan Formation. These volcanic country rocks were intensely altered to form alteration minerals such as chlorite, epidote, and actinolite. A zircon U-Pb age for the dacite is 316 ± 2 Ma (Duan et al., 2014). K-feldspar granite intruded into the volcanic country rocks at southwestern Dunde (Fig. 2B), and it yielded a zircon U-Pb age of 296 ± 1 Ma (Duan et al., 2014). Skarn occurs along the contact between basaltic-andesitic tuff and limestone (see the cross section in Fig. 2B). The deposit has a succession of superposed zones of alteration concentrically from the orebody outwards: diopside, epidote, chlorite, and carbonate. Three magnetite-bearing skarns (13DD-03, 13DD-04, and 13DD-05) were sampled at Dunde. Skarn samples consisted predominantly of diopside,
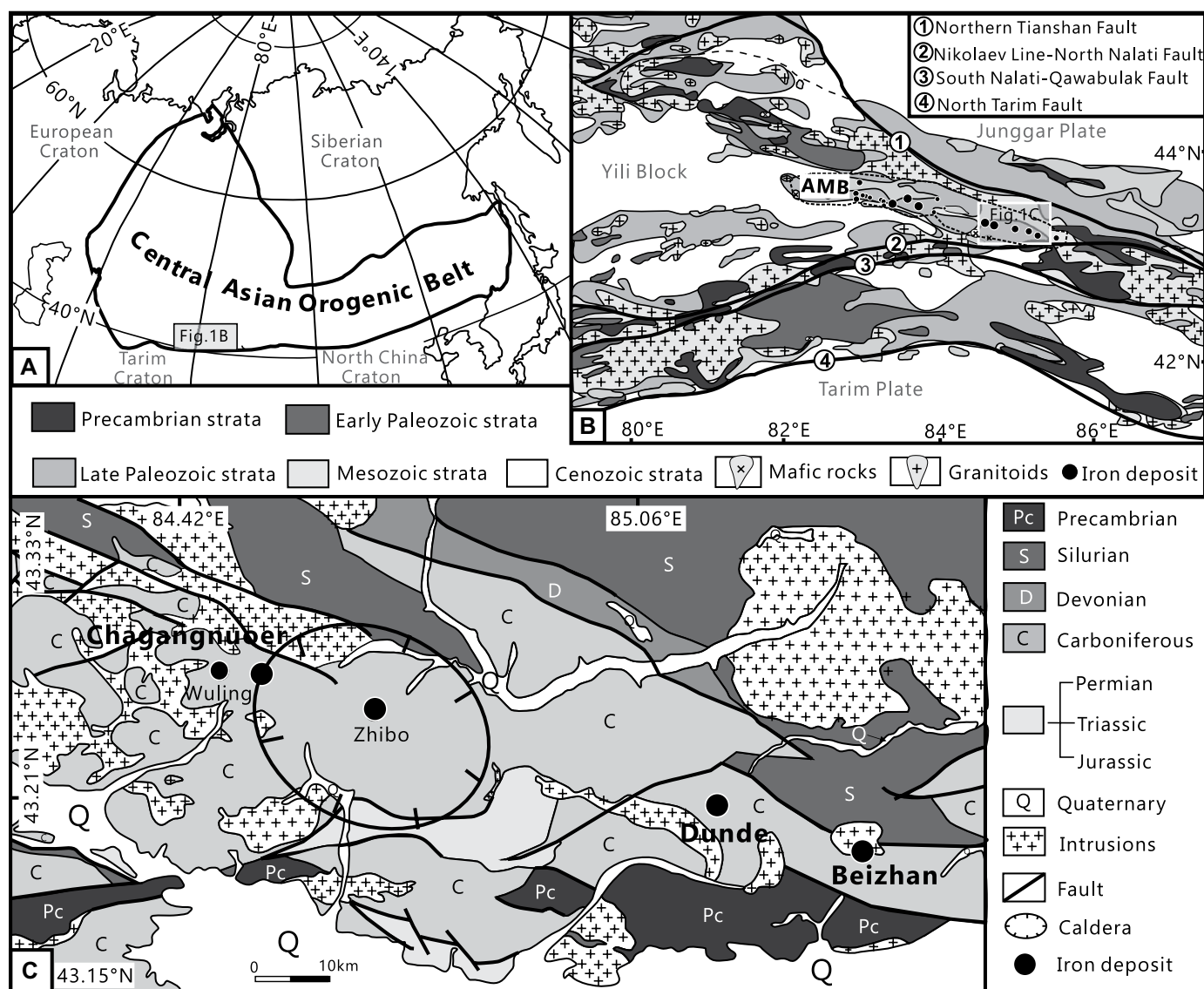
Figure 1. (A) Tectonic sketch map of the Central Asia orogenic belt (modified after Şengör et al., 1993; Jahn, 2004). (B) Geological map of the Chinese western Tianshan showing the major Fe deposits along the Awulale metallogenetic belt (AMB [black dashed line]; modified after Gao et al., 2009). (C) Geological map of the eastern Awulale metallogenetic belt (modified after Zhang et al., 2012a), showing the spatial distribution of Wuling, Chagangnuoer, Dunde, and Beizhan Fe deposits around a caldera system, centering around the Zhibo Fe deposit.

garnet, and magnetite, with lesser pyrite and calcite (Fig. 3). Garnets are honey-colored (Fig. 3), subhedral, and medium grained (Fig. 4). Magnetite is included/cemented by skarn minerals of diopside and garnet. Specially, magnetite is net-veined in skarn sample 13DD-03 (Fig. 3).
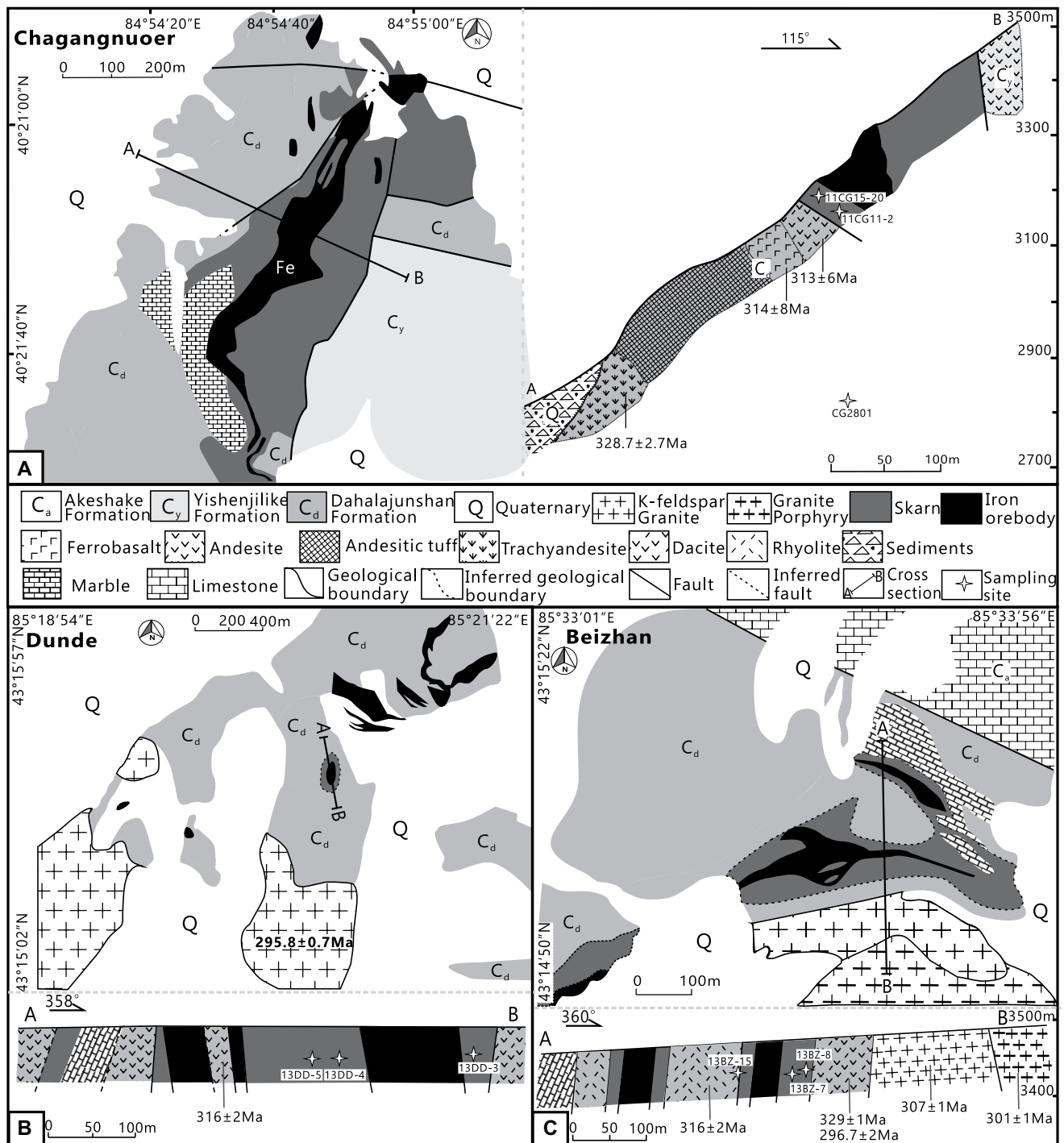
The Beizhan Fe deposit is the largest Fe deposit of the three with an iron ore reserve of ~226 Mt at 41 wt% (Fig. 2C; Zhang et al., 2012b). Country rocks include andesite, dacite, dacitic tuff, and rhyolite of the late Carboniferous Dahalajunshan and Akeshake Formations, and they are covered by Quaternary sediments. Zircon U-Pb ages for the rhyolite and dacite are 316 ± 2 Ma (Li et al., 2013) and 329 ± 1 Ma

(Sun et al., 2012), respectively. A skarn zone and limestone zone extend outward from the iron orebody, and no sharp boundaries can be identified between adjacent alteration zones. K-feldspar granite, granitic porphyry, dioritic porphyrite, and allgovite intruded the southern Beizhan district. K-feldspar granite and granite porphyry yielded zircon U-Pb ages of 307 ± 1 Ma (Sun et al., 2012) and 301 ± 1 Ma (Zheng et al., 2014), respectively. Three garnet-bearing skarn samples (13BZ-07, 13BZ-08, and 13BZ-15) were selected for in situ U-Pb dating. Samples 13BZ-07 and 13BZ-08 were taken from the altered hanging wall, while sample 13BZ-15 was taken from the footwall

of the iron orebodies. All the skarn samples were composed of light-brown garnet and dark-green hedenbergite with some pyrite (Fig. 3). Garnet grains were observed to be anhedral and included some pyrite (Fig. 4).

Taochong Garnet (TC-13)

We used the Taochong garnet (TC-13) as a matrix-matched reference material in the LA-(MC)-ICP-MS dating. The TC-13 sample was taken from an ~2 kg hand specimen of garnet skarn from the Taochong Fe deposit, located in the Fanchang district of the Middle-Lower Yangtze River Valley metallogenetic belt, South

Figure 2. Geological maps of: (A) the Chagangnuoer Fe deposit (modified after Li et al., 2015), (B) the Dunde Fe-Zn deposit (modified after Ge, 2013), and (C) the Beizhan Fe deposit (modified after Zheng et al., 2014). An orebody cross-section A–B is provided for each of the three deposits, showing the sampling locations (yellow stars) and the spatial relationship between country rocks and iron orebody. Notably, skarn sample CG2801 is a drilling-core sample and was taken from a depth of 137 m. Ages of some igneous rocks are marked on the geological maps and cross sections, and sources of these published ages are cited in the text.

China (Cao et al., 2012). The Taochong skarn consists predominantly of garnet and pyroxene with lesser actinolite, chlorite, and calcite. The garnet is mostly of giant crystal and chemically belongs to grandite ($Ad_{79.2–99.8}Gr_{0.2–20.8}$; Xu and Lin, 2000). The skarn zone at Taochong is of tabular shape, with a strike length of ~1000 m, depth of over 1000 m, and thickness of 50–150 m (Xu and Lin, 2000). The skarn formation was thought to be genetically associated with granites under the deposit (Wang et al., 2007). Granite samples recovered from drill holes are geochemically similar to widespread Mesozoic A-type granitoids (sensitive high-resolution ion microprobe zircon U-Pb dating:
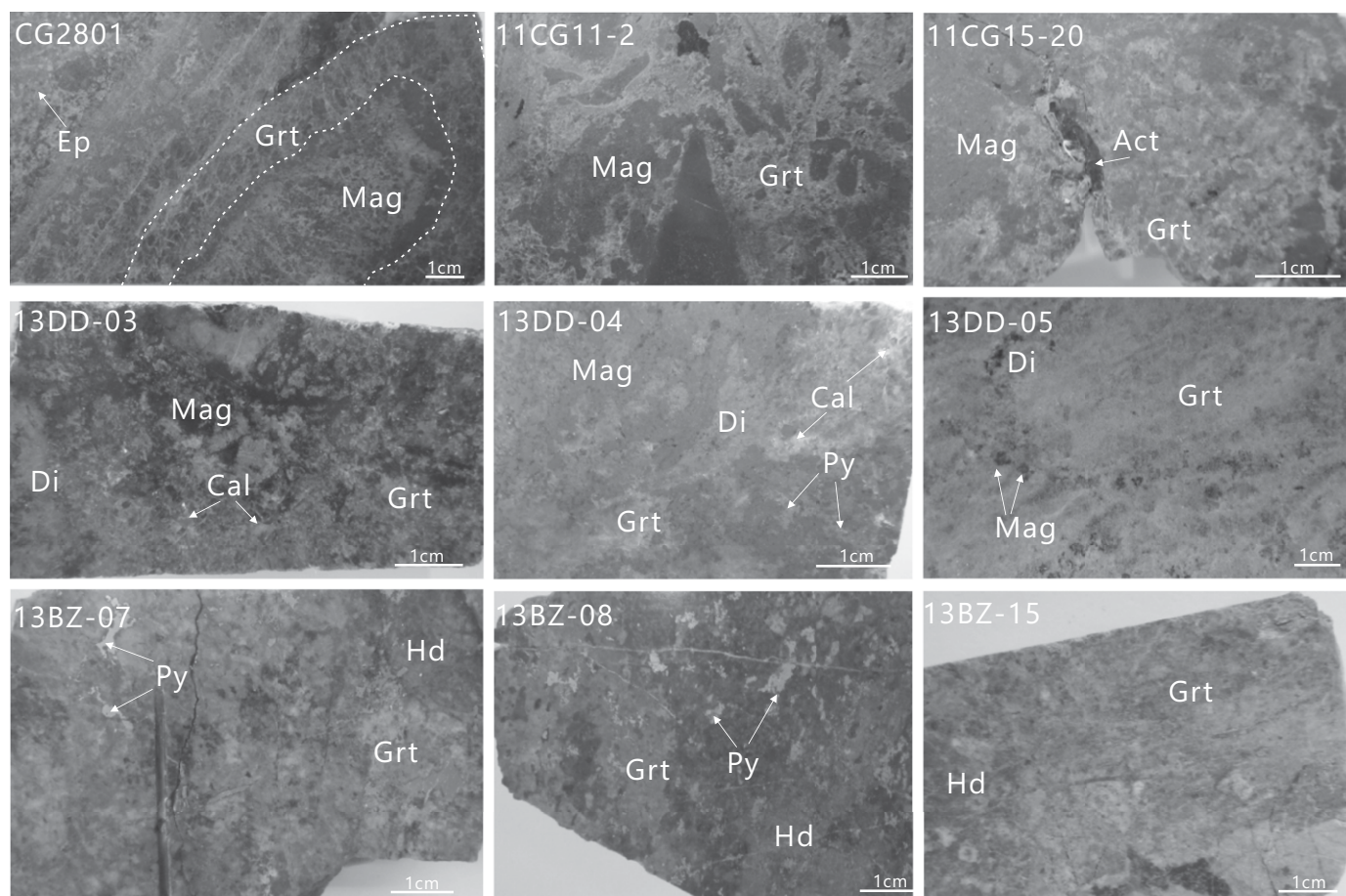
Figure 3. Hand specimens of nine studied skarns. CG2801, 11CG11-2, and 11CG15-20 come from Chagangnuoer Fe deposit, 13DD-3, 13DD-4, and 13DD-5 come from Dunde Fe-Zn deposit, and 13BZ-7, 13BZ-8, and 13BZ-15 are from Beizhan Fe deposit. Abbreviations: Grt—garnet, Di—diopside, Hd—hedenbergite, Act—actinolite, Ep—epidote, Mag—magnetite, Py—pyrite, Cal—calcite. These mineral abbreviations follow the recommendations of Whitney and Evans (2010).

125.3 ± 2.9–124.3 ± 2.5 Ma; Lou and Du, 2006) in the Fanchang area (Wang et al., 2007).

ANALYTICAL METHODS

Electron Probe Microanalyzer (Major Elements) and LA-ICP-MS (Trace Elements)

Major elements of garnets were measured by an electron probe microanalyzer (JEOL EPMA JXA-8230) equipped with five wavelength-dispersive spectrometers (WDS) at the Chinese Academy of Sciences (CAS) Key Laboratory of Mineralogy and Metallogeny, Guangzhou Institute of Geochemistry, Chinese Academy of Sciences (GIGCAS). Secondary and back-scattered electron (BSE) images were used to guide analyses on target positions of minerals. A 1 μm defocused beam was operated for analyses at an acceleration voltage of 15 kV with a beam current of 20 nA. Measured X-ray

intensities were corrected by the ZAF method using the calibration of standard minerals with various diffracting crystals (in parentheses): wollastonite for Si (TAP), corundum for Al (TAP), hematite for Fe (LiF), Mn-oxide for Mn (PET), periclase for Mg (TAP), wollastonite for Ca (PETH), and rutile for Ti (PETJ). The X-ray peak counting time for the upper and lower baselines of each element was 10 s and 5 s, respectively.

Trace elements were measured with a LA-ICP-MS (Resonetics RESOlution S-155 laser + Agilent 7900) at CAS Key Laboratory of Mineralogy and Metallogeny, GIGCAS. The laser was operated at 6 Hz repetition rate and 3.46 J/cm² energy density with 50 s ablation time and 43 μm laser spots. Multiple reference materials (NIST612, BCR-2G, BHVO-2G, and BIR-1G) were used as external calibration references, and ²⁹Si was used as an internal standard, based on mean Si concentrations of garnet from EPMA analysis. The off-line selection, integration of

the background and analytical signals, time-drift correction, and quantitative calibration were performed using ICPMSDataCal (Liu et al., 2008).

LA-ICP-MS element mapping of garnet was performed at the Ore Deposit and Exploration Centre, School of Resources and Environmental Engineering, Hefei University of Technology, Hefei, China, using a LA-ICP-MS (PhotonMachines 193 nm laser + Agilent 7900). Element maps were created by ablating sets of parallel line rasters in a grid across the sample. A laser spot size of 80 μm and a scan speed of 40 μm/s were chosen in this study. A laser repetition of 10 Hz was selected at a constant energy output of 50 mJ, resulting in an energy density of ~3 J/cm² at the target. Reference material NIST610 was analyzed for data calibration at the start and end of each mapping session. Images were compiled and processed using the program LIMS3.2 (Wang et al., 2017).
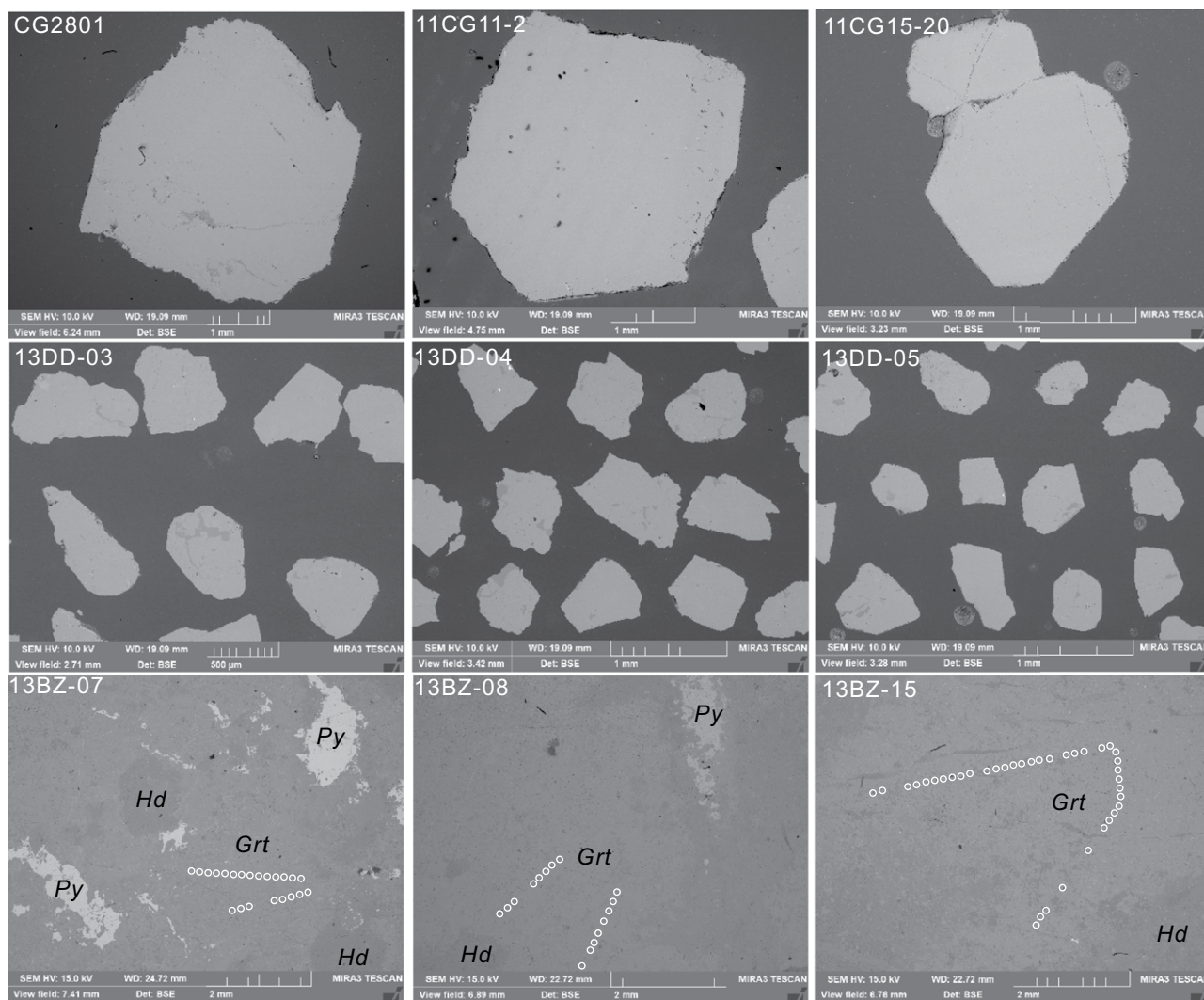
Figure 4. Backscattered electron (BSE) images of garnets and intergrown minerals in the skarns from Chagangnuoer, Dunde, and Beizhan Fe deposits. No compositional zoning is seen on these garnet BSE images, indicating homogeneous chemical compositions of major elements. White circles marked on the BSE images represent the positions of laser spots. Abbreviations are the same to those in Figure 3.

Solution Pb-Pb Isochron Dating

The Taochong garnet samples (TC-13) were first crushed to millimeter-scale grains. Only inclusion- and crack-free grains were selected under the microscope for the solution Pb-Pb dating. About 350 mg of Taochong garnet was ultrasonically cleaned in Milli-Q pure water for 60 min (15 min for each time, repeated four times). Samples were then dried on a hotplate of 40 °C and subdivided into 11 aliquots of ~30 mg each. These garnet aliquots were stepwise dissolved after being treated with HBr, HCl, and HF solutions and their mixtures. All dissolutions were dried out on a hotplate at 90 °C and then dissolved with 500 μL of 1.2 *N* HBr solution for Pb separation through AG1 × 8 anion exchange columns. Pb isotopes were measured on a Nu Plasma high-resolution MC-ICP-MS at the Radiogenic Isotope Facility, School of Earth and Environmental Sciences, University of Queensland, Brisbane, Australia. A ^{205}Tl/^{203}Tl standard solution was used for mass fractionation corrections, and the NBS-981 standard was used for long-term drift corrections. The same approach was also applied to measuring the Pb isotopic compositions in four Taochong calcite subsamples, which were taken from the same skarn as the analyzed garnet.

U-Pb Dating by LA-(MC)-ICP-MS

Both garnet grain mounts and garnet-bearing thin sections were used for U-Pb dating. All samples were first ultrasonicated in detergent solution for 1 h and then washed with Milli-Q water for at least three times and then dried out on a 40 °C hotplate in order to remove any surface contamination as much as possible. Transmitted light pictures, reflected light pictures, and BSE pictures were used to locate inclusion- and crack-free spots for the in situ laser analyses. U-Pb isotopic measurement was conducted using a Nu Plasma II MC-ICP-MS or a Thermo iCap-RQ quadrupole ICP-MS (for cross-calibration of high-U garnet standards), equipped with an ASI RESOlution SE 193 nm ArF-excimer laser at the Radiogenic Isotope Facility, School of Earth and Environmental Sciences, University of Queensland, Brisbane, Australia. The Nu Plasma II MC-ICP-MS consists of 15 Faraday cups and 5 secondary electron multipliers capable of static collection of all ^{238}U-^{232}Th-^{208}Pb-^{207}Pb-^{206}Pb-^{204}(Pb, Hg)-^{202}Hg ion beams.

Figure 5. (A) Pb-Pb isochron plot of the Taochong garnet (TC-13). (B) Procedure for normalization of sample ^{238}U/^{206}Pb using the measured array of TC-13 garnet as the primary reference material. Notes: The *x* intercepts of these arrays were calculated using Isoplot v. 3.75 (Ludwig, 2012) as X_{RM} and X_{UM}, referring to the measured *x* intercepts of the TC-13 reference material and unknown, respectively. A line anchored to the initial common Pb projected through the correct age for the TC-13 garnet gives an *x* intercept of X_{RC}. X_{UC} refers to the corrected *x* intercept of the unknown. Linear correction factor: $f = X_{RC}/X_{RM} \approx$ (True Age)$_{TC-13}$/(Measured Age)$_{TC-13}$, where $X_{UC} = X_{UM} \times f$. MSWD—mean square of weighted deviates.

The laser was operated with 25 s or 30 s of ablation time, 10 Hz repetition rate, and 3.0 J/cm² energy density. Both 64 µm and 100 µm laser spot sizes were employed to maximize count rates and optimize precisions, since U contents of most garnet samples were sub–part per million to several parts per million. When coupled with the Nu Plasma II MC-ICP-MS, a typical working sensitivity of 400,000–800,000 cps/ppm ^{238}U signal was achieved with a 100 µm laser spot size. When coupled with the iCap-RQ Q-ICP-MS, the corresponding sensitivity is ~10 times lower. We used NIST614 as the primary reference material to correct for ^{207}Pb/^{206}Pb fractionation and for instrument drift in the ^{238}U/^{206}Pb ratio (Woodhead and Hergt, 2010), but not for down-hole fractionation. The ^{238}U/^{206}Pb ratios of garnets were calibrated with a matrix-matched reference material, the Taochong garnet (TC-13: 126.2 ± 2.3 Ma; illustrated in the next section and Fig. 5A), using the calibration methods suggested by Chew et al. (2014) (see Fig. 5B). Qichun and Dongping garnets independently dated to 130 ± 2 Ma and 388 ± 4 Ma by Deng et al. (2017) were used to monitor accuracy of analytical procedures. Raw data reduction was completed using Iolite software_v3.64 (Paton et al., 2011). Garnet U-Pb ages were calculated with the online IsoplotR program (Vermeesch, 2018).

RESULTS

Pb-Pb Isochron Age and Initial Common Pb of the Taochong Garnet (TC-13)

The Taochong garnet (TC-13) has U contents of 21.1–44.7 ppm, Th contents of 0.02–0.27 ppm, and Pb contents of 0.64–1.54 ppm (Table 1), with ^{206}Pb/^{204}Pb ratios from 72.2180 ± 0.0044 to 180.5873 ± 0.0378, ^{207}Pb/^{204}Pb ratios from 18.2419 ± 0.0012 to 23.5146 ± 0.0049, and ^{208}Pb/^{204}Pb ratios from 38.0781 ± 0.0085 to 38.7494 ± 0.0034. The Pb-Pb isochron age was obtained as 126.2 ± 2.3 Ma (mean square of weighted deviates [MSWD] = 4.2; Fig. 5A). This age is analytically indistinguishable from the zircon U-Pb age (125.3 ± 2.9 Ma; Lou and Du, 2006) of the granitic protolith in the Fanchong ore district.

The analyzed calcite displayed an intergrowth relationship with garnet, indicative of coprecipitation from the same parental fluid. The Taochong calcite subsamples have extremely low U contents (0.21–5.76 ppb), which are <0.01% of U contents in Taochong garnets. Therefore, the radiogenic Pb components are negligible in calcite, and their Pb isotopes approximate the initial Pb isotopic compositions. A weighted average value of calcite ^{207}Pb/^{206}Pb compositions was obtained as 0.845 ± 0.022 (2σ), which represents the initial ^{207}Pb/^{206}Pb composition of TC-13 garnet.

LA-ICP-MS Mapping of Garnet TC-13

A 3 mm × 5 mm grain of TC-13 garnet was selected for element mapping. Element maps are shown in Figure 6, and related concentration data are summarized in Table 2. Element maps display obvious concentration zones for selected elements. Fe, Al, and Mn maps display the same zoning pattern, consistent with their isomorphism in the tetrahedral site of the garnet lattice (Gaspar et al., 2008). Fe concentrations

TABLE 1. PB-PB ISOTOPIC DATA FROM THE GARNET AND CALCITE IN SAMPLE TC-13 FROM TAOCHONG SKARN FE DEPOSIT

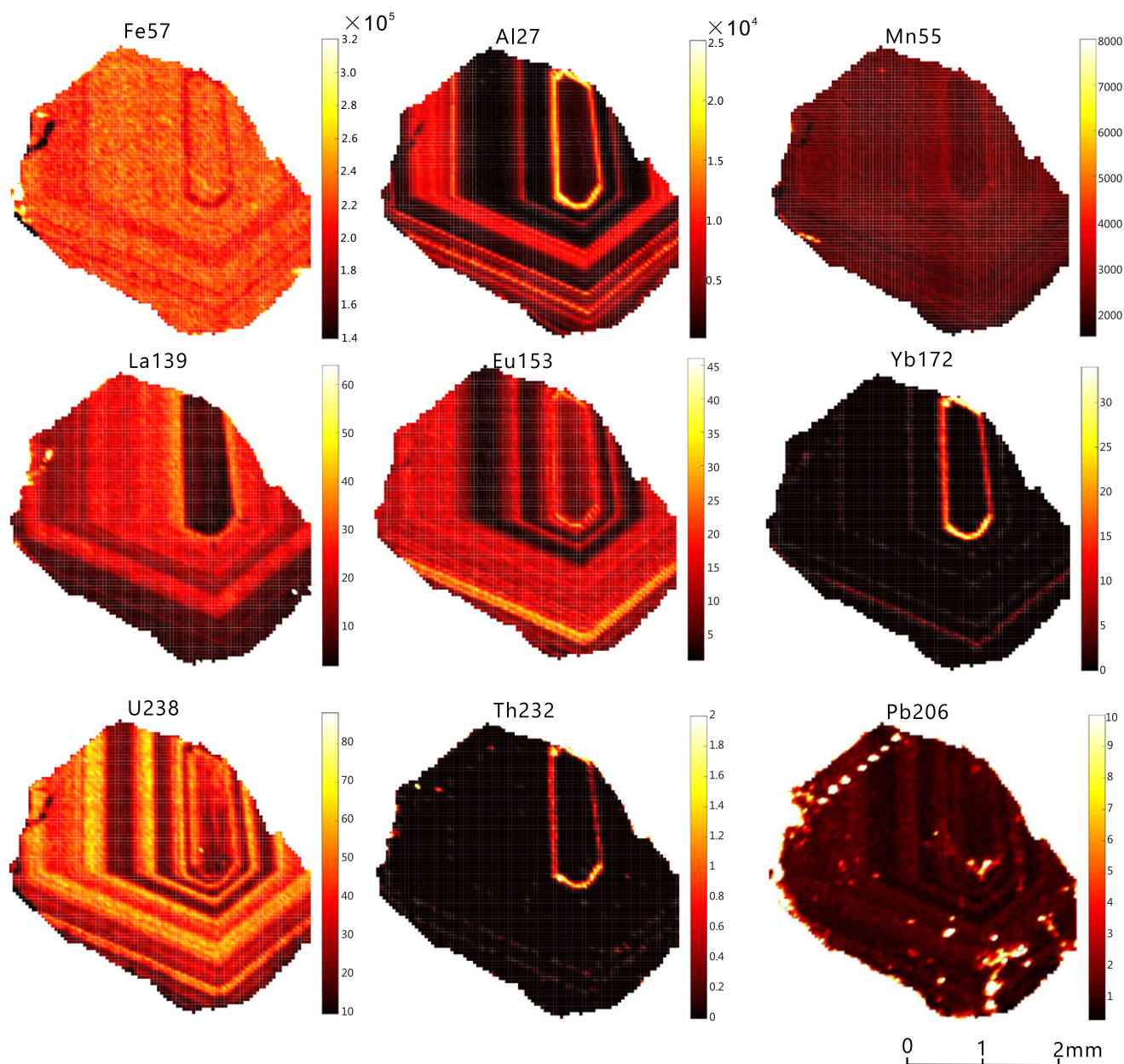| Sample no.	Mineral	U (ppm)	Th (ppm)	Pb (ppm)	208Pb/204Pb	2σ	207Pb/204Pb	2σ	206Pb/204Pb	2σ	208Pb/206Pb	2σ	207Pb/206Pb	2σ
TC13-01	Garnet	42.7	0.046	1.060	38.5938	0.0077	23.5146	0.0049	180.5873	0.0378	0.213713	0.000005	0.130209	0.000003
TC13-02	Garnet	44.7	0.161	1.540	38.6661	0.0039	19.1978	0.0018	91.8773	0.0088	0.420842	0.000008	0.208951	0.000003
TC13-03	Garnet	41.0	0.064	1.230	38.6075	0.0042	20.3068	0.0034	114.6462	0.0135	0.336742	0.000005	0.177115	0.000003
TC13-04	Garnet	34.5	0.071	0.917	38.6270	0.0051	22.2010	0.0042	153.6516	0.0228	0.251392	0.000007	0.144494	0.000003
TC13-05	Garnet	30.8	0.274	1.080	38.7494	0.0034	19.0936	0.0017	89.7076	0.0097	0.431924	0.000008	0.212835	0.000002
TC13-06	Garnet	33.3	0.049	1.130	38.0781	0.0085	20.6404	0.0043	121.9824	0.0222	0.312223	0.000008	0.169238	0.000051
TC13-07	Garnet	30.4	0.029	0.784	38.5468	0.0044	22.7294	0.0077	164.6511	0.1372	0.234029	0.000212	0.137975	0.000003
TC13-08	Garnet	26.2	0.037	0.999	38.5600	0.0028	18.4397	0.0013	76.2949	0.0051	0.505402	0.000010	0.241686	0.000003
TC13-09	Garnet	25.3	0.033	0.795	38.5453	0.0029	19.8329	0.0013	104.9304	0.0070	0.367314	0.000010	0.189015	0.000004
TC13-10	Garnet	25.1	0.049	0.997	38.5770	0.0028	18.2419	0.0012	72.2180	0.0044	0.534164	0.000011	0.252596	0.000003
TC13-11	Garnet	21.1	0.022	0.641	38.5178	0.0046	20.0701	0.0023	109.8729	0.0091	0.350540	0.000008	0.182657	0.000065
TC13-12	Calcite	0.003	0.002	0.107	38.4724	0.0161	15.6400	0.0065	18.4047	0.0078	2.089958	0.000170	0.849614	0.000065
TC13-13	Calcite	0.006	0.002	0.093	38.5128	0.0154	15.6423	0.0047	18.4545	0.0053	2.086802	0.000080	0.847505	0.000027
TC13-14	Calcite	0.001	0.001	0.090	38.5767	0.0154	15.6523	0.0060	18.7489	0.0073	2.057372	0.000053	0.834900	0.000032
TC13-15	Calcite	0.000	0.001	0.112	38.5979	0.0102	15.6404	0.0038	18.4306	0.0047	2.094269	0.000072	0.848578	0.000026

Figure 6. Laser ablation–inductively coupled plasma–mass spectrometry (LA-ICP-MS) element maps of a garnet grain of TC-13. Concentrations in each scale bar are in ppm. Notably, on the Pb map, bright (high-Pb) areas represent previously ablated holes (see spot line on the top left) or surface cracks, and significant common Pb was incorporated in these holes and cracks. However, over 97% of the mapping area has Pb contents <5 ppm.

TABLE 2. CONCENTRATIONS (PPM) OF MAJOR AND TRACE ELEMENTS FROM THE MAPPED GARNET SUBSAMPLE OF TC-13

Element	Min	Max	Mean	2SD
Fe(57)	142,935	316,217	233,640	21,943
Al(27)	148	25,309	4543	4439
Mn(55)	1520	7683	2430	295
La(139)	1.7	63.9	17.0	7.4
Eu(153)	0.9	27.2	11.1	5.8
Yb(172)	0	33.5	0.6	2.6
U(238)	11.2	88.0	39.5	15.1
Th(232)	0	1.89	0.02	0.12
Pb(206)	0.3	9.6	1.2	0.9

Note: The mass number in brackets refers to the isotope measured. 2SD means double standard deviations of the mean.

are 50–100 times higher than and negatively correlated with those of Al and Mn, favoring their andradite-dominant composition. As for REEs, the garnet is enriched in light (L) REEs (see La map) but contains low contents of heavy (H) REEs (see Yb map), consistent with the typical REE pattern of andradite (Jamtveit and Hervig, 1994; Smith et al., 2004). U and Pb also exhibit evident concentration zoning, with their concentrations varying from 11 to 88 ppm and from 0.3 to 9.6 ppm (Table 1), respectively. However, in situ U-Pb isotopic data indicate

that TC-13 shows fairly good U-Pb isotopic homogeneity, with over 95% of ^{238}U/^{206}Pb ratios clustering around 49.8 ± 0.8 (2σ; Table DR1[1]), which is consistent with our observation of the same zoning patterns for ^{238}U and ^{206}Pb (Fig. 6).

[1]GSA Data Repository item 2019339, Tables DR1–DR3, is available at http://www.geosociety.org/datarepository/2019 or by request to editing@geosociety.org.
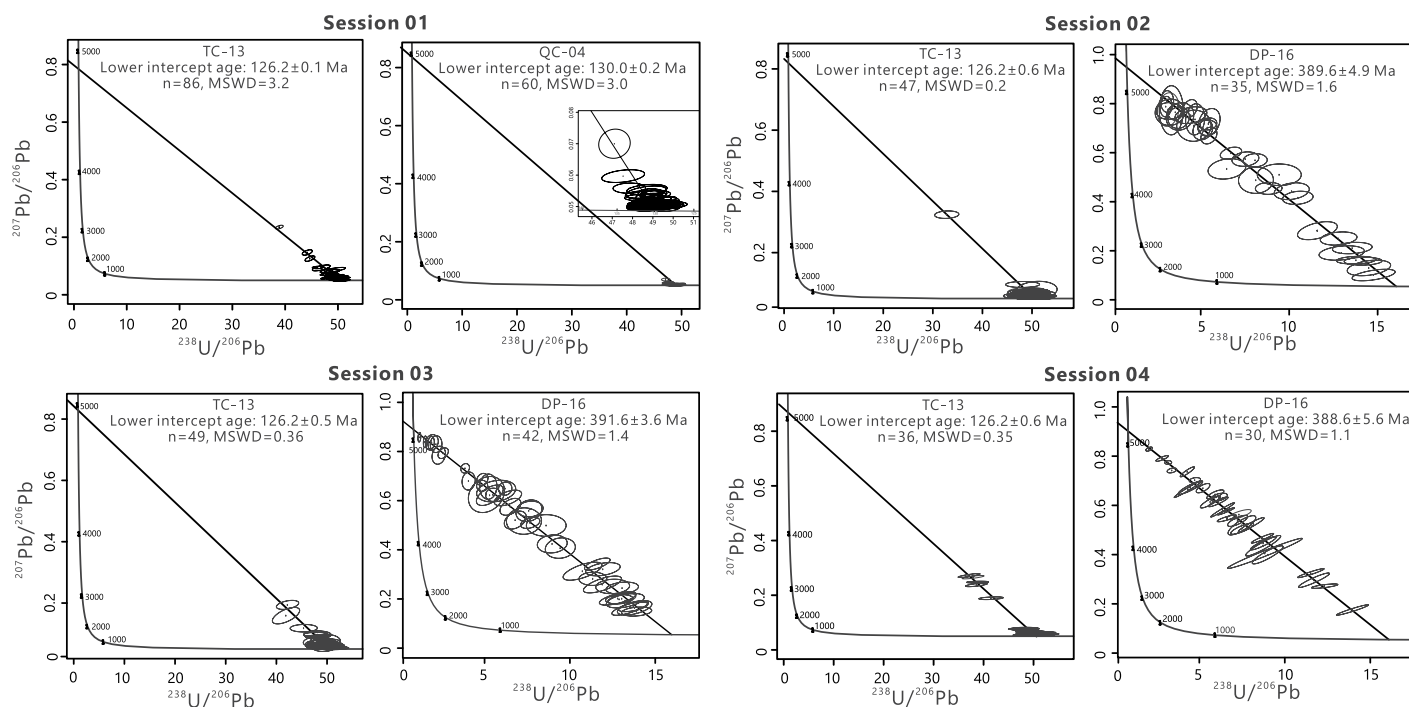
Figure 7. U-Pb data plotted on Tera-Wasserburg concordia for the Taochong (TC-13), Qichun (QC-04), and Dongping (DP-16) garnets in four different sessions. Uncertainties and ellipses of single analyses are at two standard deviations (2σ). MSWD—mean square of weighted deviates.

In Situ U-Pb Ages of Awulale Garnets

Using the TC-13 garnet as the reference material and QC-04 and DP-16 as monitoring garnet standards (Table DR1; Fig. 7) for U-Pb dating, U-Pb isotopic compositions were obtained from garnets from Chagangnuoer (CG2801, 11CG11-2, and 11CG15-20), Dunde (13DD-03, 13DD-04, and 13DD-05), and Beizhan (13BZ-07, 13BZ-08, and 13BZ-15; Table DR2 [see footnote 1]; Fig. 8). U-Pb isotopic data from single-spot analyses are plotted as a linear array on the Tera-Wasserburg concordia diagram and allow us to report a lower-intercept age for each sample.

In total, 61 analyses for sample CG2801 have U contents from 0.37 ppm to 1.89 ppm (0.80 ppm on average) and produce a lower-intercept $^{206}Pb/^{238}U$ age of 326.1 ± 3.3 Ma (MSWD = 0.5); 86 analyses for sample 11CG11-

2 give U contents from 0.13 ppm to 1.18 ppm (0.49 ppm on average) and yield a lower-intercept $^{206}Pb/^{238}U$ age of 312.5 ± 1.7 Ma (MSWD = 0.1); and 75 analyses for sample 11CG15-20 have U contents from 0.40 ppm to 1.20 ppm (0.73 ppm on average) and produce a lower-intercept $^{206}Pb/^{238}U$ age of 316.3 ± 2.9 Ma (MSWD = 0.2).

In total, 60 analyses for sample 13DD-3 give U contents from 0.81 ppm to 6.19 ppm (3.10 ppm on average) and produce a lower-intercept $^{206}Pb/^{238}U$ age of 295.6 ± 1.0 Ma (MSWD = 1.4); 86 analyses for sample 13DD-4 have U contents from 0.34 ppm to 3.51 ppm (1.79 ppm on average) and yield a lower-intercept $^{206}Pb/^{238}U$ age of 313.8 ± 2.7 Ma (MSWD = 1.0); and 78 analyses for sample 13DD-5 give U contents from 0.18 ppm to 5.39 ppm (2.49 ppm on average) and produce a lower-intercept $^{206}Pb/^{238}U$ age of 311.2 ± 2.4 Ma (MSWD = 0.3).

In total, 125 analyses for sample 13BZ-7 have U contents from 0.64 to 15.4 ppm (3.37 ppm on average) and produce a lower-intercept $^{206}Pb/^{238}U$ age of 314.7 ± 1.7 Ma (MSWD = 1.0); 97 analyses on sample 13BZ-8 give U contents from 0.22 to 2.11 ppm (0.92 ppm on average) and yield a lower-intercept $^{206}Pb/^{238}U$ age of 329.0 ± 5.1 Ma (MSWD = 0.6); and 93 analyses for sample 13BZ-15 have U contents from 0.49 to 3.74 ppm (1.62 ppm on average) and yield a lower-intercept $^{206}Pb/^{238}U$ age of 314.2 ± 3.5 Ma (MSWD = 0.7).

Major Elements and REEs of Awulale Garnets

The compositions of the Chagangnuoer, Dunde, and Beizhan garnets range from $Ad_{45.3}Gr_{50.0}$ to $Ad_{62.2}Gr_{33.3}$, from $Ad_{28.7}Gr_{54.1}$

TABLE 3. SUMMARY OF U-PB DATING CONDITIONS AND RESULTS OF GARNET REFERENCE MATERIALS IN FOUR DIFFERENT SESSIONS

Session	Date	Instrument	Laser conditions	Uncorrected U-Pb age and common Pb of TC-13	Uncorrected U-Pb age and common Pb of monitor garnets	Corrected U-Pb age of TC-13 (Ma)	Corrected U-Pb age of monitor garnets (Ma)
01	20171120	LA-MC-ICP-MS	Laser time: 30 s; Spot size: 64 μm	132.4 ± 0.1 Ma; 0.80 ± 0.02	136.1 ± 0.1 Ma; 0.85 ± 0.03 (QC-04)	126.2 ± 0.1	130.0 ± 0.2
02	20180202	LA-Q-ICP-MS	Laser time: 25 s; Spot size: 100 μm	121.8 ± 0.6 Ma; 0.83 ± 0.05	375.9 ± 4.8 Ma; 0.95 ± 0.01 (DP-16)	126.2 ± 0.6	389.4 ± 4.9
03	20180203	LA-Q-ICP-MS	Laser time: 25 s; Spot size: 100 μm	121.9 ± 0.5 Ma; 0.84 ± 0.08	378.8 ± 3.4 Ma; 0.94 ± 0.01 (DP-16)	126.2 ± 0.5	392.1 ± 3.0
04	20180207	LA-MC-ICP-MS	Laser time: 25 s; Spot size: 100 μm	121.6 ± 0.6 Ma; 0.89 ± 0.03	374.7 ± 5.4 Ma; 0.95 ± 0.01 (DP-16)	126.2 ± 0.6	388.6 ± 3.5

Note: Laser ablation–multicollector–inductively coupled plasma–mass spectrometer (LA-MC-ICP-MS) was an ASI RESOlution 193 nm excimer laser with a Nu Plasma II multicollector ICP-MS, and LA-Q-ICMS represents an ASI RESOlution 193 nm excimer laser with a Thermo iCap RQ quadrupole ICP-MS.
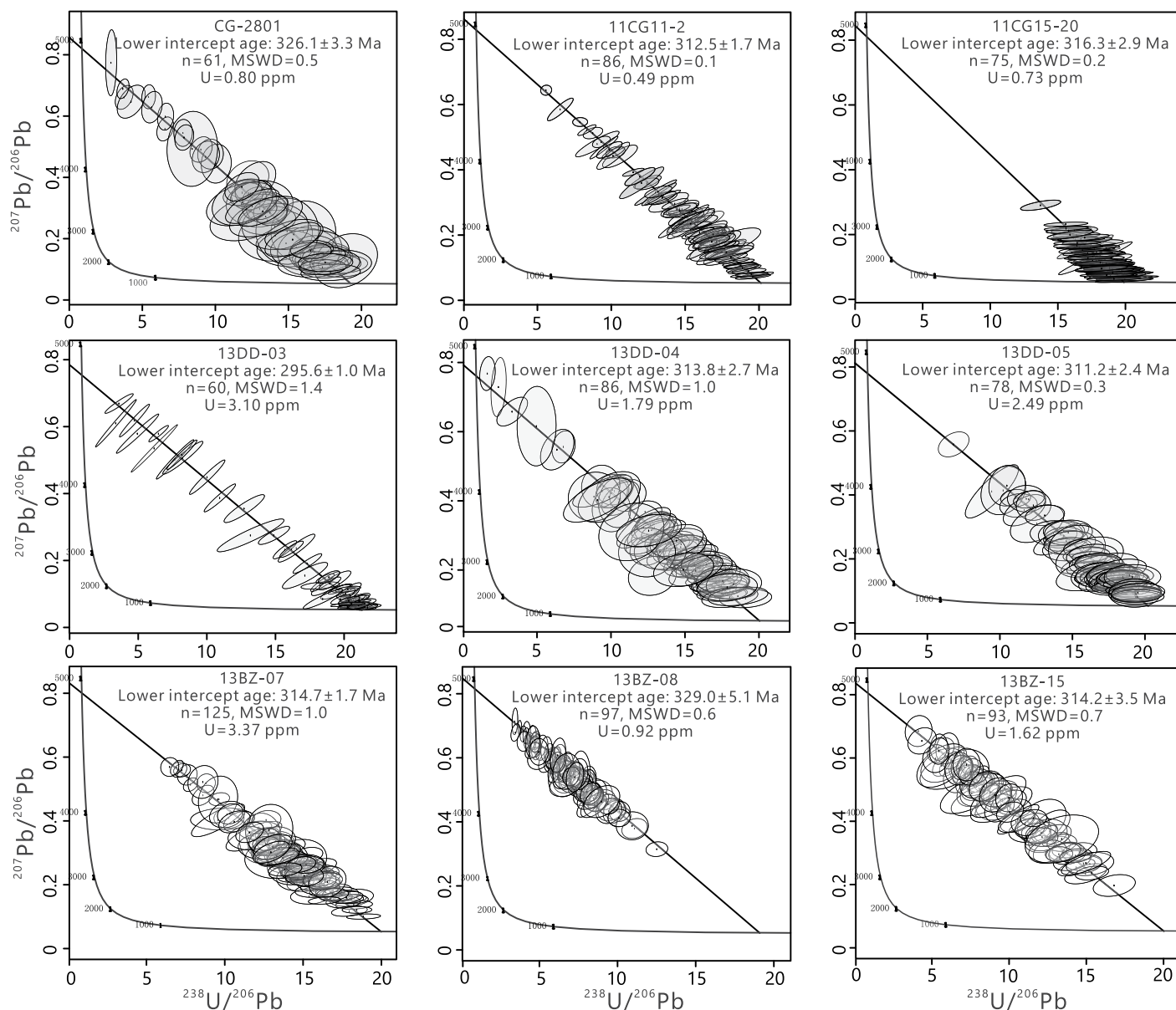
Figure 8. Garnet U-Pb data plotted on Tera-Wasserburg concordia for Chagangnuoer, Dunde, and Beizhan Fe deposits. Average U contents of each garnet sample are also shown. Uncertainties and ellipses of single analyses are at two standard deviations (2σ). MSWD—mean square of weighted deviates.

to $Ad_{41.3}Gr_{65.3}$, and from $Ad_{19.7}Gr_{71.1}$ to $Ad_{36.8}Gr_{57.3}$, respectively, with lesser almandine, spessartine, and pyrope components (Table DR3 [see footnote 1]; Fig. 9). All these skarn garnets chemically belong to the grandite series. Their compositions are relatively clustered within the same deposit but show some variations between different deposits, with andradite proportions decreasing from Chagangnuoer, to Dunde, to Beizhan deposits.

REE compositions in the same sample are also clustered but show some variations between different samples (Table DR3 [see foot-

note 1]; Fig. 9). Chagangnuoer garnets yield similar REE distribution patterns with depleted LREEs, flat HREEs, and slight Eu anomalies (δEu: 0.71–1.56). Dunde and Beizhan garnets have two types of REE patterns. Similar to Chagangnuoer garnets, garnets in samples 13DD-3 and 13BZ-15 also display depleted LREEs, flat HREEs, and slight Eu anomalies (δEu: 0.94–1.48 for 13DD-3, 0.66–1.16 for 13BZ-15). However, garnet REE patterns in the other four samples are convex-up in LREEs, with maxima at Nd and positive Eu anomalies (δEu: 1.63–4.88 for 13DD-4 and 13DD-5, 1.26–4.46 for 13BZ-7 and 13BZ-8).

DISCUSSION

Taochong Garnet (TC-13) as a Reference Material

Instead of being homogeneously distributed, ^{238}U and ^{206}Pb concentrations exhibited obvious zoning on element maps of TC-13 garnet (Fig. 6). However, as suggested by in situ U-Pb isotopic data, TC-13 only shows modest U-Pb isotopic heterogeneity, with over 95% of corrected $^{238}U/^{206}Pb$ ratios clustering around 49.8 ± 0.8 (2σ), implying that ^{206}Pb is predominantly radiogenic, and its distribution in garnet is con-
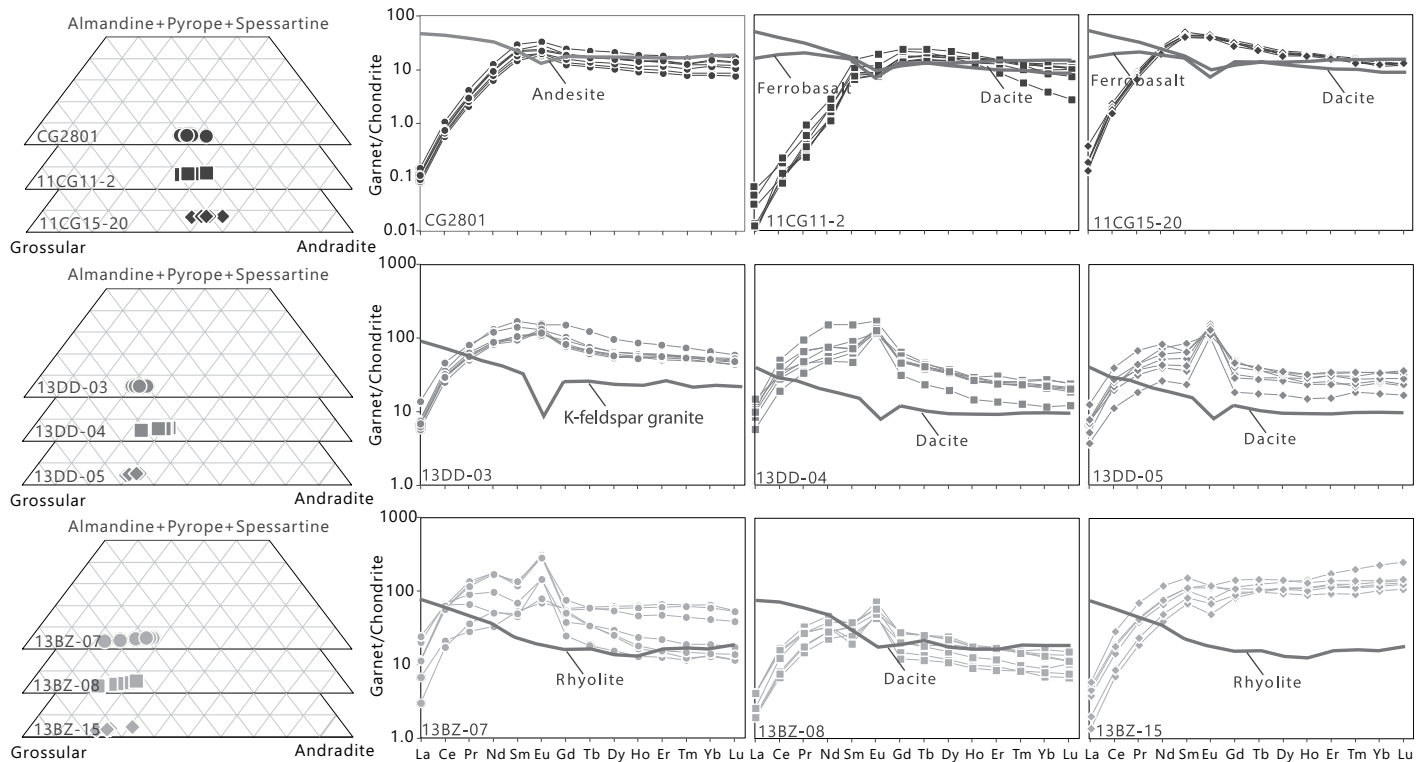
Figure 9. Component ternary diagrams and chondrite-normalized rare earth element (REE) distribution patterns of garnets from the Chagangnuoer, Dunde, and Beizhan deposits. The REE patterns of potential source rocks were employed for comparison with coeval garnets at each locality.

sistent with the ^{238}U distribution. Notably, due to the similar geochemical behaviors between U (mainly U^{4+}) and REEs in grandite lattice (Gaspar et al., 2008; Smith et al., 2004), the zoning patterns of U are somewhat similar to those of REEs (especially Eu), demonstrating that U in TC-13 garnet is mainly structure-bound and that the U-Pb garnet dating provides direct constraints on the timing of garnet crystallization.

On the Tera-Wasserburg plots, U-Pb isotopic compositions of TC-13 form a mixing array between initial and radiogenic Pb (Fig. 7). The common Pb proportion of TC-13 is only ~3% on average, up to 6% of total Pb. Following the approach suggested by Chew et al. (2014) and Roberts et al. (2017), U-Pb normalization can be achieved using the Taochong garnet (TC-13) as the reference material. A linear correction factor was calculated with the measured Tera-Wasserburg intercept age and the true age of TC-13 (line correction factor: $f = X_{RC}/X_{RM} \approx [\text{True Age}]_{TC-13}/[\text{Measured Age}]_{TC-13}$; the specific method is shown in detail in Figure 5B and its notes). The same correction factor was then applied to correcting ^{238}U/^{206}Pb ratios of other garnets in the same analytical session to obtain their ages. We tested the robustness of using TC-13 as a reference material by analyzing Qichun and Dongping garnets with independently known ages in four separate sessions

under different analytical conditions on multiple days (Table 3). U-Pb dating of TC-13 in four sessions yielded uncorrected Tera-Wasserburg lower-intercept ages of 132.5 ± 0.1 Ma, 121.8 ± 0.6 Ma, 121.9 ± 0.5 Ma, and 121.6 ± 0.6 Ma (Table 3). The obtained four Tera-Wasserburg upper intercepts for TC-13 were all within the error range of its initial ^{207}Pb/^{206}Pb ratio (0.845 ± 0.022) obtained by the solution method. After ^{238}U/^{206}Pb corrections with the TC-13 (126.2 Ma), corrected Tera-Wasserburg lower-intercept ages of Qichun and Dongping garnets were 130.0 ± 0.2 Ma for QC-04 in session 01, and 389.6 ± 4.9 Ma, 391.6 ± 3.6 Ma, and 388.6 ± 5.6 Ma for DP-16 in sessions 02–04 (Table 3; Fig. 7), consistent with ages reported by Deng et al. (2017). The U-Pb age reproducibility of the Qichun and Dongping garnets indicates that TC-13 garnet is a reliable reference material for in situ U-Pb dating, and the obtained U-Pb ages of the unknown samples are also expected to be highly reliable.

U-Pb Ages and REE Geochemistry of Awulale Garnets: Constraints on Igneous Protoliths and Fluid Properties

The average U contents of the nine analyzed garnets ranged from 0.49 ppm to 3.37 ppm, with only four of them containing sub–part per

million U contents. These garnets were dated with a LA-MC-ICP-MS instrument, which can achieve a working sensitivity of 400,000–800,000 cps/ppm ^{238}U signal for a 100 μm laser spot. Their age precisions are in the range of 0.3% to 1.6%, highlighting the advantage of the LA-MC-ICP-MS technique in dating low-U minerals. The U-Pb ages of the nine garnet samples from the three deposits could be divided into three groups: 329.0 ± 5.1–326 ± 3.3 Ma (two samples), 316.3 ± 2.9–311.2 ± 2.4 Ma (six samples), and 295.6 ± 1.0 Ma (one sample), respectively, implying three episodes of skarn alteration in the volcanic-hosted iron mineralization system of the eastern Awulale metallogenic belt (Fig. 10). Based on the age distributions, the first episode of skarn alteration was seen in the Chagangnuoer and Beizhan deposits, and the second occurred in all three deposits, while the third was only present in the Dunde deposit. By comparing garnet ages and their spatial distributions with those of the adjacent igneous rocks, the potential igneous protoliths of each episode of skarn alteration can be determined. At Chagangnuoer, all the skarns formed earlier than the adjacent granites (250 ± 1 Ma and 305 ± 1.3 Ma; Sun et al., 2015) in the ore district and thus could not be genetically related to these granites. Instead, the earlier episode of skarn alteration was coeval with the 328.7 ± 2.7 Ma andesite,
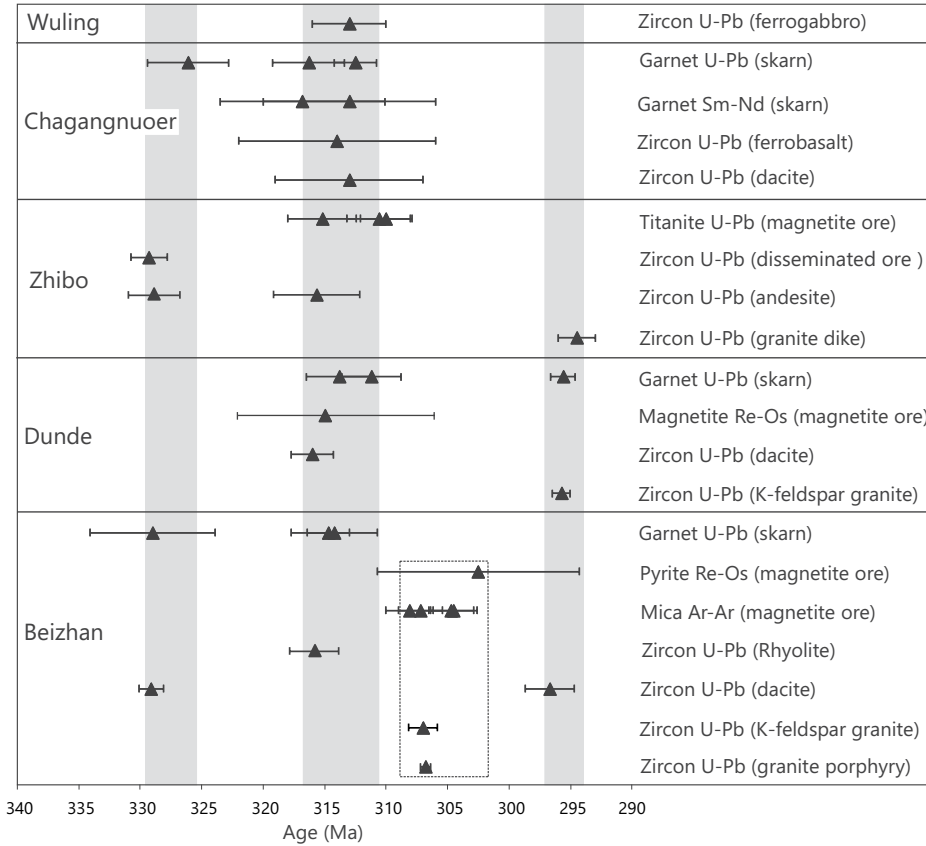
Figure 10. Comparisons between garnet U-Pb ages and other ore-related ages reported in the eastern Awulale metallogenic belt. Gray shades highlight the durations of the three episodes of skarn alteration. Data sources: ages for the Wuling Fe deposit from Yan et al. (2015); ages for the Chagangnuoer Fe deposit from Hong et al. (2012), Li et al. (2015), and Zhang et al. (2015); ages for the Dunde Fe-Zn deposit from Duan et al. (2014) and Yang et al. (2016); ages for the Beizhan Fe deposit from Zheng et al. (2014), Sun et al. (2012), and Duan et al. (2018).
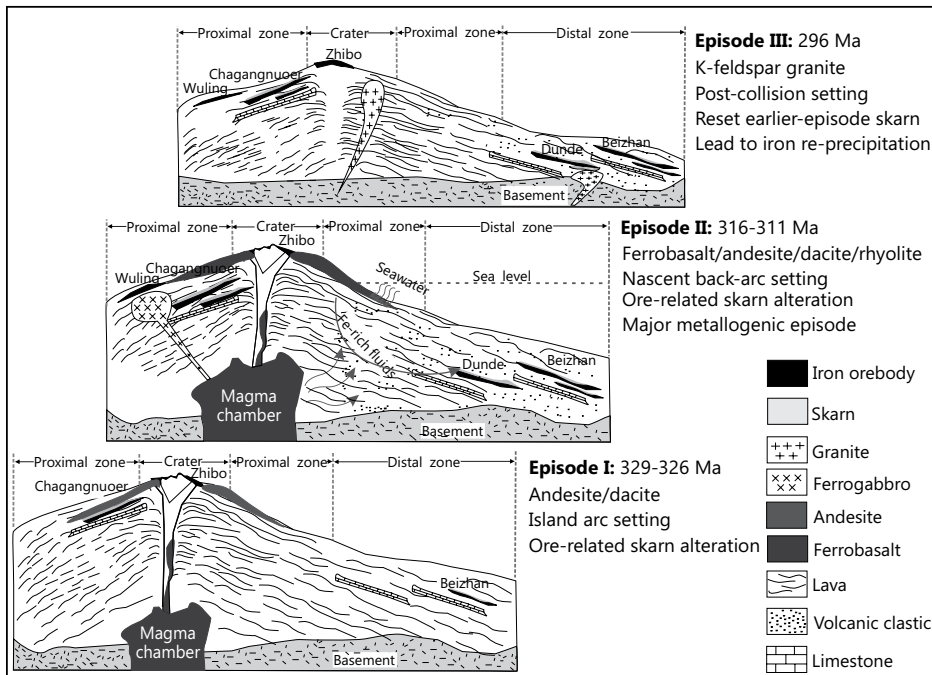
Figure 11. Cartoon showing the multiple-episode metallogenic models for the volcanic-hosted iron mineralization system in the eastern Awulale metallogenetic belt, western Tianshan, Central Asia.

whereas the younger episode agrees in age with the 314 ± 8 Ma ferrobasalt and the 313 ± 6 Ma dacite in adjacent volcanic country rocks. At Dunde, the two episodes of skarn alteration were contemporary with the 316 ± 2 Ma dacite in adjacent country rocks and the 295.8 ± 0.7 Ma K-feldspar granite intruding the southern ore district, respectively. At Beizhan, instead of being related to adjacent granites (307 ± 1 Ma and 301 ± 1 Ma; Sun et al., 2012; Zheng et al., 2014) in the ore district, the two episodes of skarn alteration were more likely associated with the 329 ± 1 Ma dacite and the 316 ± 2 Ma rhyolite in the region. Most importantly, our field observation indicates that these neighboring volcanic rocks themselves have experienced different degrees of skarn alteration to form minerals including actinolite, epidote, and chlorite, supporting the argument that these volcanic rocks or their intrusive counterparts may have provided the heat source and hydrothermal fluids for skarn formation.

The REE patterns of the Awulale garnets show some variations between different samples (Fig. 9). Most garnets typically exhibit LREE depletion and a flat HREE pattern, which are present in all three deposits, while several garnets from the Dunde and Beizhan deposits showed convex-up

LREE patterns with Nd maxima and positive Eu anomalies. REE compositions of skarn minerals primarily originate from their igneous and carbonate protoliths, and the former is the major REE contributor for skarns (Whitney and Olmsted, 1998). However, the REE concentrations and patterns of the studied garnets differ dramatically from their potential igneous protoliths, which show LREE-enriched patterns with typical negative Eu anomalies (Fig. 9), indicative of substantial REE mobility and modification during garnet crystallization. Smith et al. (2004) and Gaspar et al. (2008) suggested that variations in REE patterns of skarn garnets are closely associated with the proportional changes of the major components, whereby grossular-rich garnets display typical REE patterns of depleted LREEs and flat HREEs, while andradite-rich garnets have REE patterns showing convex-up LREE patterns with Nd maxima and positive Eu anomalies. However, the two types of garnets in Dunde and Beizhan have similar mineral chemistry (Fig. 9), precluding the major component variations as a possible control. Generally, garnets with the HREE-enriched patterns form in near equilibrium with their parent fluids, with low water/rock (W/R) ratios (Park et al., 2017; Xu et al., 2016); in contrast, garnets with LREE-enriched patterns grow as the result of introduction of externally buffered fluids with high W/R ratios, and surface adsorption has a major control on the REE incorporation into garnets (Gaspar et al., 2008; Whitney and Olmsted, 1998). Therefore, REE patterns of garnets mainly reflect the W/R ratios and resultant REE incorporation mechanisms during garnet precipitation. Moreover, an obvious difference between the two types of REE patterns lies in their Eu anomalies, which are determined by the relative proportions of Eu^{2+} versus Eu^{3+} in fluids. Eu^{2+} is predominant at temperatures above 250 °C (Bau, 1991; Sverjensky, 1984), and the stability of soluble Eu^{2+} is strengthened by chlorine solutions (Mayanovic et al., 2007). The coexistence of magnetite and pyrite with Dunde and Beizhan garnets (13DD-4, 13DD-5, 13BZ-7, and 13BZ-8) suggests a reduced fluid environment with fO_2 below the hematite-magnetite buffer. Microthermometry results of fluid inclusions and the occurrences of abundant chlorine-rich minerals (like ferropargasite and apatite) in these deposits indicated that ore-forming fluids were predominantly chlorine solutions, including $NaCl-H_2O$, $CaCl_2-H_2O$, $FeCl_2-H_2O$. and brine-featured aqueous systems (Duan et al., 2014; Yan et al., 2018). In such a reduced and high-temperature skarn system (370–700 °C; Meinert, 1992), Eu^{2+} dominates over Eu^{3+} in fluids, leading to a positive Eu shift relative to adjacent REEs and positive Eu anomalies in their REE patterns. Moreover, U solubility is sensitive to fO_2 variation (Smith et al., 2004), and the reduced fluid condition would decrease U

contents in hydrothermal solutions and promote more U^{4+} incorporation into garnets (McLennan and Taylor, 1979; ValsamiJones and Ragnarsdottir, 1997). This accords with the results that these garnet samples (13DD-4, 13DD-5, 13BZ-7, and 13BZ-8) have higher U contents than the other coeval ones.

Implications for Metallogenesis

Skarn ages, as constrained from garnet U-Pb dates, provide significant insights into metallogenesis, especially the timing of iron mineralization, because skarn and ore minerals display good coexisting relationships in all three deposits in this study (Figs. 2 and 3). For the first episode of skarn alteration, ore minerals like magnetite and pyrite are present in the 329.0 ± 5.1–326 ± 3.3 Ma skarns and coexist with garnet crystals as inclusions or intergrowths (Fig. 3), demonstrating that this episode of skarn alteration was associated with iron mineralization. Meanwhile, zircon U-Pb dating of a disseminated ore from Zhibo gave an analytically indistinguishable age of 329.9 ± 1.5 Ma, supporting this episode of iron mineralization in the eastern Awulale metallogenetic belt. For the second episode, six of the nine garnet U-Pb ages cluster between 316.3 ± 2.9 and 311.2 ± 2.4 Ma (Fig. 10), and the ore-bearing features of these skarns indicate that this episode was also metallogenic. Additionally, Re-Os isochron dating of the Dunde magnetite gave an age of 314 ± 12 Ma (Yang et al., 2016). Titanite U-Pb dating of a Zhibo magnetite ore yielded three ages between 315.2 ± 2.8 Ma and 310 ± 2.1 Ma (Jiang et al., 2018). All these ages suggest that the main iron mineralization occurred between 316 Ma and 310 Ma. Magnetite was also found to be present in the third episode of skarn dated to 295.6 ± 1.0 Ma, implying that this episode of skarn alteration was also related to iron mineralization. It is also likely that the net-veined magnetite (13DD-3 in Fig. 3) was a product of early-episode magnetite dissolution and remobilization. Further work on geochronology and geochemistry of these magnetite veins is needed to assess the metallogenic potential of this episode of skarn alteration.

Though various metallogenic models have been proposed for the volcanic-hosted iron deposits in the eastern Awulale metallogenetic belt, the establishment of these models was largely based on the observation of individual deposits and the knowledge of only one episode of skarn alteration and iron mineralization (Duan et al., 2014; Sun et al., 2015; Yan et al., 2018). Our results indicate that three episodes of skarn alteration and at least two episodes of iron mineralization have taken place in the re-

gion. Notably, for the same episode of skarn alteration, we identified different types of igneous protoliths in different deposits, varying from basaltic to rhyolitic compositions. In fact, coeval magmatic (mainly volcanic) rocks are also exposed in other volcanic-hosted Fe deposits of the eastern Awulale metallogenetic belt, such as the 328.7 ± 2.1 Ma and 316.3 ± 3.4 Ma andesite, and 294.5 ± 1.5 Ma K-feldspar granite at Zhibo (Jiang et al., 2014, 2018; Zhang et al., 2012a), 313 ± 3 Ma ferrogabbro at Wuling (Yan et al., 2015), and 296.7 ± 2.0 Ma dacite at Beizhan (Sun et al., 2012). The absence of contemporary skarn alterations in these deposits may be attributed to incomplete sampling of their skarns, or more likely to unsuitable host rocks for skarn formation in such areas. Above all, we propose that, instead of being related to a certain igneous rock, the skarn alterations in these deposits were probably triggered by multiple periods of intrusive/extrusive magmatic activities, where magmatic hydrothermal fluids generated by these igneous rocks interacted with the carbonate rocks to develop abundant skarn deposits. Given the close spatial relationship of the five deposits around the same crater, it is necessary to consider the skarn alteration and iron mineralization of these deposits as one interrelated system.

In summary, we envisage that a multiple-episode metallogenic model may better depict the metallogenic processes of the volcanic-hosted iron mineralization system in the eastern Awulale metallogenetic belt (Fig. 11). The first episode of skarn formation and mineralization, distributed in the Zhibo, Chagangnuoer, and Beizhan deposits, was genetically related to the 329 Ma andesite and dacite in an island-arc setting (Jiang et al., 2014; Sun et al., 2012). Skarns formed through contact metasomatism between these intermediate-acidic volcanic rocks (or subvolcanic intrusions underneath the volcanic sequence) and surrounding limestone. Meanwhile, Fe-rich magmatic-hydrothermal fluids may have also precipitated magnetite along the volcanic-limestone contact. The second episode of skarn alteration and mineralization was widespread in all five volcanic-hosted iron deposits, associated with a variety of volcanic rocks, including ferrobasalt, andesite, dacite, and rhyolite (or subvolcanic intrusions underneath the volcanic sequence), in a nascent back-arc rifting setting (Li et al., 2015; Yan et al., 2015). The skarn genesis is interpreted to have been similar to the last episode and formed as a result of contact metasomatism. In particular, the extensional back-arc setting favored upwelling of high-density ferrobasaltic magmas (like the Chagangnuoer ferrobasalt and Wuling ferrogabbro) in this episode. The ferrobasaltic magma may have provided the original iron for region-scale iron mineralization via heated and recycled Fe-rich

ore fluids. The third episode of skarn alteration occurred only at Dunde and was caused by the Permian K-feldspar granite intrusion (Duan et al., 2014; Ge, 2013). The coeval K-feldspar granites formed in a postcollision setting and usually occur as small dikes in the ore district. However, they neither have any contact with orebodies nor exhibit any evidence of alteration based on our field observation, arguing against the 295 Ma K-feldspar granite as the causative intrusion for the skarn formation. An alternative interpretation for the third episode of skarn formation is that the thermal effect of the intruded magma reactivated earlier episodes of iron mineralization, and the 295.6 Ma garnet records the reset of an earlier garnet U-Pb isotopic system (closure temperature: ~800 °C for ~0.5-cm-diameter garnet grains; Mezger et al., 1989).

CONCLUSIONS

LA-MC-ICP-MS U-Pb dating techniques were employed to date low-U garnets from multi-episode skarns within the volcanic-hosted iron deposits of the eastern Awulale metallogenetic belt, western Tianshan, Central Asia. In conjunction with trace-element data and published results, the following major conclusions can be drawn:

(1) Taochong garnet (TC-13) has a Pb-Pb isochron age of 126.2 ± 2.3 Ma with an initial $^{207}Pb/^{206}Pb$ ratio of 0.845 ± 0.022. It has relatively low but nonnegligible common Pb (~3% on average, up to 6% of total Pb). Our study demonstrates that this garnet can be used as a new matrix-matched reference material for LA-(MC)-ICP-MS dating of garnets.

(2) High-precision (0.3%–1.6%) U-Pb ages were obtained for low-U garnets from the eastern Awulale metallogenetic belt, highlighting the advantage of LA-MC-ICP-MS techniques in dating low-U minerals.

(3) Three episodes of skarn alteration, i.e., 329.0 ± 5.1–326 ± 3.3 Ma (2 samples), 316.3 ± 2.9–311.2 ± 2.4 Ma (6 samples), and 295.6 ± 1.0 Ma (1 sample), occurred in the volcanic-hosted Fe deposits of the eastern Awulale metallogenetic belt. The former two episodes of skarn alteration were associated with coeval magmatic-hydrothermal activity and have economic mineralization. The third episode was possibly caused by the emplacement of coeval K-feldspar granite, but its metallogenic potential deserves further assessment.

(4) The Awulale garnets show two types of REE patterns. The first group displays depleted LREE and flat HREE patterns, which may result from formation near equilibrium with their parent fluids under conditions of low W/R ratios. The other group displays a convex-up LREE pattern with Nd maxima and positive Eu anoma-

lies, which may have formed as a result of surface adsorption under conditions of high W/R ratios. Positive Eu anomalies and relative higher U contents in garnets also imply more reduced fluid conditions for their precipitation.

REFERENCES CITED

Allen, M.B., Windley, B.F., and Zhang, C., 1993, Palaeozoic collisional tectonics and magmatism of the Chinese Tien Shan, Central Asia: Tectonophysics, v. 220, no. 1–4, p. 89–115, https://doi.org/10.1016/0040-1951(93)90225-9.

Bau, M., 1991, Rare-earth element mobility during hydrothermal and metamorphic fluid-rock interaction and the significance of the oxidation state of europium: Chemical Geology, v. 93, no. 3–4, p. 219–230, https://doi.org/10.1016/0009-2541(91)90115-8.

Baxter, E.F., and Scherer, E.E., 2013, Garnet geochronology: Timekeeper of tectonometamorphic processes: Elements, v. 9, no. 6, p. 433–438, https://doi.org/10.2113/gselements.9.6.433.

Cao, Y., Du, Y., Gao, F., Hu, L., Xin, F., and Pang, Z., 2012, Origin and evolution of hydrothermal fluids in the Taochong iron deposit, Middle–Lower Yangtze Valley, eastern China: Evidence from microthermometric and stable isotope analyses of fluid inclusions: Ore Geology Reviews, v. 48, p. 225–238, https://doi.org/10.1016/j.oregeorev.2012.03.009.

Cheng, H., Vervoort, J.D., Dragovic, B., Wilford, D., and Zhang, L., 2018, Coupled Lu-Hf and Sm-Nd geochronology on a single eclogitic garnet from the Huwan shear zone, China: Chemical Geology, v. 476, p. 208–222, https://doi.org/10.1016/j.chemgeo.2017.11.018.

Chew, D.M., Sylvester, P.J., and Tubrett, M.N., 2011, U-Pb and Th-Pb dating of apatite by LA-ICPMS: Chemical Geology, v. 280, no. 1, p. 200–216, https://doi.org/10.1016/j.chemgeo.2010.11.010.

Chew, D.M., Petrus, J.A., and Kamber, B.S., 2014, U-Pb LA-ICPMS dating using accessory mineral standards with variable common Pb: Chemical Geology, v. 363, no. 1, p. 185–199, https://doi.org/10.1016/j.chemgeo.2013.11.006.

Deng, X.-D., Li, J.-W., Luo, T., and Wang, H.-Q., 2017, Dating magmatic and hydrothermal processes using andradite-rich garnet U-Pb geochronometry: Contributions to Mineralogy and Petrology, v. 172, no. 9, p. 71, https://doi.org/10.1007/s00410-017-1389-2.

Duan, S., Zhang, Z., Jiang, Z., Zhao, J., Zhang, Y., Li, F., and Tian, J., 2014, Geology, geochemistry, and geochronology of the Dunde iron-zinc ore deposit in western Tianshan, China: Ore Geology Reviews, v. 57, p. 441–461, https://doi.org/10.1016/j.oregeorev.2013.08.019.

Duan, S., Zhang, Z., Wang, D., Jiang, Z., Luo, W., and Li, F., 2018, Pyrite Re-Os and muscovite $^{40}Ar/^{39}Ar$ dating of the Beizhan iron deposit in the Chinese Tianshan orogen and its geological significance: International Geology Review, v. 60, no. 1, p. 57–71, https://doi.org/10.1080/00206814.2017.1318721.

Feng, J.X., Shi, F.P., Wang, B.Y., Hu, J.M., Wang, J.T., and Tian, J.Q., 2010, Volcanogenic Iron Deposits in

the Awulale Metallogenic Belt in Western Tianshan: Beijing, Geological Publishing House, p. 16–112.

Gao, J., Long, L., Klemd, R., Qian, Q., Liu, D., Xiong, X., Su, W., Liu, W., Wang, Y., and Yang, F., 2009, Tectonic evolution of the South Tianshan orogen and adjacent regions, NW China: Geochemical and age constraints of granitoid rocks: International Journal of Earth Sciences, v. 98, no. 6, p. 1221–1238, https://doi.org/10.1007/s00531-008-0370-8.

Gaspar, M., Knaack, C., Meinert, L.D., and Moretti, R., 2008, REE in skarn systems: A LA-ICP-MS study of garnets from the Crown Jewel gold deposit: Geochimica et Cosmochimica Acta, v. 72, no. 1, p. 185–205, https://doi.org/10.1016/j.gca.2007.09.033.

Ge, S.S., 2013, Characteristics and Genesis of the Dunde Iron Deposit in Xinjiang Province [master's thesis]: Beijing, China, China University of Geosciences, 28 p.

Gevedon, M., Seman, S., Barnes, J.D., Lackey, J.S., and Stockli, D.F., 2018, Unraveling histories of hydrothermal systems via U-Pb laser ablation dating of skarn garnet: Earth and Planetary Science Letters, v. 498, p. 237–246, https://doi.org/10.1016/j.epsl.2018.06.036.

Grant, J.A., 1986, The isocon diagram—A simple solution to Gresens equation for metasomatic alteration: Economic Geology and the Bulletin of the Society of Economic Geologists, v. 81, no. 8, p. 1976–1982, https://doi.org/10.2113/gsecongeo.81.8.1976.

Hong, W., Zhang, Z.H., Li, H.Q., Li, F.M., and Liu, X.Z., 2012, Metallogenic epoch of Chagangnuoer iron deposit in western Tianshan Mountains, Xinjiang: Information from garnet Sm-Nd isochron age: Mineralium Deposita, v. 31, no. 5, p. 1067–1074.

Hou, T., Zhang, Z., Pirajno, F., Santosh, M., Encarnacion, J., Liu, J., Zhao, Z., and Zhang, L., 2014, Geology, tectonic settings and iron ore metallogenesis associated with submarine volcanism in China: An overview: Ore Geology Reviews, v. 57, no. 1, p. 498–517, https://doi.org/10.1016/j.oregeorev.2013.08.007.

Jahn, B.-M., 2004, The Central Asian orogenic belt and growth of the continental crust in the Phanerozoic, in Malpas, J., Fletcher, C.J.N., Ali, J.R., and Aitchison, J.C., eds., Aspects of the Tectonic Evolution of China: Geological Society [London] Special Publication 226, p. 73–100, https://doi.org/10.1144/GSL.SP.2004.226.01.05.

Jamtveit, B., and Hervig, R.L., 1994, Constraints on transport and kinetics in hydrothermal systems from zoned garnet crystals: Science, v. 263, no. 5146, p. 505–508, https://doi.org/10.1126/science.263.5146.505.

Jansson, N.F., and Allen, R.L., 2013, Timing and setting of skarn and iron oxide formation at the Smaltarmossen calcic iron skarn deposit, Bergslagen, Sweden: Mineralium Deposita, v. 48, no. 3, p. 313–339, https://doi.org/10.1007/s00126-012-0432-5.

Jiang, Z.S., Zhang, Z.H., Wang, Z.H., Duan, S.G., Li, F.M., and Tian, J.Q., 2014, Geology, geochemistry, and geochronology of the Zhibo iron deposit in the western Tianshan, NW China: Constraints on metallogenesis and tectonic setting: Ore Geology Reviews, v. 57, p. 406–424, https://doi.org/10.1016/j.oregeorev.2013.09.016.

Jiang, Z.S., Wang, D., Zhang, Z., Duan, S., Kang, Y., and Li, F., 2018, Application of in situ titanite U-Pb geochronology to volcanic-hosted magnetite deposit: New constraints on the timing and genesis of the Zhibo deposit, western Tianshan, NW China: Ore Geology Reviews, v. 95, p. 325–341, https://doi.org/10.1016/j.oregeorev.2018.03.001.

Jung, S., and Mezger, K., 2003, U-Pb garnet chronometry in high-grade rocks—Case studies from the central Damara orogen (Namibia) and implications for the interpretation of Sm-Nd garnet ages and the role of high U-Th inclusions: Contributions to Mineralogy and Petrology, v. 146, no. 3, p. 382–396, https://doi.org/10.1007/s00410-003-0506-6.

Li, D.-p., Du, Y.-s., Pang, Z.-s., Tu, Q.-j., Zhang, Y.-p., Ge, S.-s., Shen, L.-j., and Wang, K.-h., 2013, Zircon U-Pb chronology and geochemistry of Carboniferous volcanic rocks in Awulale area, western Tianshan Mountains: Acta Geoscientica Sinica, v. 34, no. 2, p. 176–192.

Li, N.-B., Niu, H.-C., Zhang, X.-C., Zeng, Q.-S., Shan, Q., Li, C.-Y., Yan, S., and Yang, W.-B., 2015, Age, petrogenesis and tectonic significance of the ferrobasalts in the Chagangnuoer iron deposit, western Tianshan:

International Geology Review, v. 57, no. 9–10, p. 1218–1238, https://doi.org/10.1080/00206814.2015.1004136.

Liu, H., Wang, B., Shu, L., Jahn, B.-m., and Iizuka, Y., 2014, Detrital zircon ages of Proterozoic meta-sedimentary rocks and Paleozoic sedimentary cover of the northern Yili block: Implications for the tectonics of microcontinents in the Central Asian orogenic belt: Precambrian Research, v. 252, p. 209–222, https://doi.org/10.1016/j.precamres.2014.07.018.

Liu, Y., Hu, Z., Gao, S., Guenther, D., Xu, J., Gao, C., and Chen, H., 2008, In situ analysis of major and trace elements of anhydrous minerals by LA-ICP-MS without applying an internal standard: Chemical Geology, v. 257, no. 1–2, p. 34–43, https://doi.org/10.1016/j.chemgeo.2008.08.004.

Lou, Y.E., and Du, Y.S., 2006, Characteristics and zircon SHRIMP U-Pb ages of the Mesozoic intrusive rocks in Fanchang, Anhui Province: Geochimica, v. 35, no. 4, p. 359–366.

Ludwig, K., 2012, Isoplot/Ex, v. 3.75: Berkeley Geochronology Center Special Publication 5, 75 p.

Mayanovic, R.A., Anderson, A.J., Bassett, W.A., and Chou, I.M., 2007, On the formation and structure of rare-earth element complexes in aqueous solutions under hydrothermal conditions with new data on gadolinium aqua and chloro complexes: Chemical Geology, v. 239, no. 3, p. 266–283, https://doi.org/10.1016/j.chemgeo.2006.10.004.

McLennan, S.M., and Taylor, S.R., 1979, Rare earth element mobility associated with uranium mineralization: Nature, v. 282, no. 5736, p. 247–250, https://doi.org/10.1038/282247a0.

Meinert, L.D., 1992, Skarns and skarn deposits: Geoscience Canada, v. 19, no. 4, p. 145–162.

Meinert, L.D., Dipple, G.M., and Nicolescu, S., 2005, World skarn deposits: Economic Geology, 100th anniversary volume, p. 299–336.

Mezger, K., Hanson, G.N., and Bohlen, S.R., 1989, U-Pb systematics of garnet: dating the growth of garnet in the late Archean Pikwitonei granulite domain at Cauchon and Natawahunan Lakes, Manitoba, Canada: Contributions to Mineralogy and Petrology, v. 101, no. 2, p. 136–148.

Morgan, D.J., 1990, Geochemistry and mineralogy of rare earth minerals: Clay Minerals, v. 25, no. 4, p. 545–545, https://doi.org/10.1180/claymin.1990.025.4.13.

Park, C., Song, Y., Kang, I.-M., Shim, J., Chung, D., and Park, C.-S., 2017, Metasomatic changes during periodic fluid flux recorded in grandite garnet from the Weondong W-skarn deposit, South Korea: Chemical Geology, v. 451, p. 135–153, https://doi.org/10.1016/j.chemgeo.2017.01.011.

Paton, C., Hellstrom, J., Paul, B., Woodhead, J., and Hergt, J., 2011, Iolite: Freeware for the visualisation and processing of mass spectrometric data: Journal of Analytical Atomic Spectrometry, v. 26, no. 12, p. 2508–2518, https://doi.org/10.1039/c1ja10172b.

Roberts, N.M.W., Rasbury, E.T., Parrish, R.R., Smith, C.J., Horstwood, M.S.A., and Condon, D.J., 2017, A calcite reference material for LA-ICP-MS U-Pb geochronology: Geochemistry Geophysics Geosystems, v. 18, no. 7, p. 2807–2814, https://doi.org/10.1002/2016GC006784.

Salnikova, E.B., Stifeeva, M.V., Chakhmouradian, A.R., Glebovitsky, V.A., and Reguir, E.P., 2018, The U-Pb system in schorlomite from calcite–amphibole–pyroxene pegmatite of the Afrikanda Complex (Kola Peninsula): Doklady Earth Sciences, v. 478, no. 2, p. 148–151, https://doi.org/10.1134/S1028334X18020083.

Scherer, E.E., Cameron, K.L., and Blichert-Toft, J., 2000, Lu-Hf garnet geochronology: Closure temperature relative to the Sm-Nd system and the effects of trace mineral inclusions: Geochimica et Cosmochimica Acta, v. 64, no. 19, p. 3413–3432, https://doi.org/10.1016/S0016-7037(00)00440-3.

Seman, S., Stockli, D.F., and McLean, N., 2017, U-Pb geochronology of grossular-andradite garnet: Chemical Geology, v. 460, p. 106–116, https://doi.org/10.1016/j.chemgeo.2017.04.020.

Şengör, A.M.C., Natalin, B.A., and Burtman, V.S., 1993, Evolution of the Altaid tectonic collage and Paleozoic crustal growth in Eurasia: Nature, v. 364, no. 6435, p. 299–307, https://doi.org/10.1038/364299a0.

Shannon, R.D., 1976, Revised effective ionic radii and systematic studies of interatomic distances in halides and chalcogenides: Acta Crystallographica, v. 32, p. 751–767, https://doi.org/10.1107/S0567739476001551.

Simonetti, A., Heaman, L.M., Chacko, T., and Banerjee, N.R., 2006, In situ petrographic thin section U-Pb dating of zircon, monazite, and titanite using laser ablation–MC–ICP-MS: International Journal of Mass Spectrometry, v. 253, no. 1, p. 87–97, https://doi.org/10.1016/j.ijms.2006.03.003.

Smit, M.A., Scherer, E.E., and Mezger, K., 2013, Lu-Hf and Sm-Nd garnet geochronology: Chronometric closure and implications for dating petrological processes: Earth and Planetary Science Letters, v. 381, no. 4, p. 222–233, https://doi.org/10.1016/j.epsl.2013.08.046 (corrigendum: http://dx.doi.org/10.1016/j.epsl.2014.02.015).

Smith, M.P., Henderson, P., Jeffries, T.E.R., Long, J., and Williams, C.T., 2004, The rare earth elements and uranium in garnets from the Beinn an Dubhaich aureole, Skye, Scotland, UK: Constraints on processes in a dynamic hydrothermal system: Journal of Petrology, v. 45, no. 3, p. 457–484, https://doi.org/10.1093/petrology/egg087.

Sun, J.-m., Ma, Z.-p., Xu, X.-y., Li, X.-y., Weng, K., and Zhang, T., 2012, The formation epoch of the host wall rock of the Beizhan iron deposit in west Tianshan Mountains of Xinjiang and its geological significance: Geological Bulletin of China, v. 31, no. 12, p. 1973–1982.

Sun, W.L., Niu, Y.L., Ma, Y.X., Liu, Y., Zhang, G.R., Hu, Z.X., Zhang, Z.W., Chen, S., Li, J.Y., Wang, X.H., and Gong, H.M., 2015, Petrogenesis of the Chagangnuoer deposit, NW China: A general model for submarine volcanic-hosted skarn iron deposits: Science Bulletin, v. 60, no. 3, p. 363–379, https://doi.org/10.1007/s11434-014-0684-9.

Sverjensky, D.A., 1984, Europium redox equilibria in aqueous solution: Earth and Planetary Science Letters, v. 67, no. 1, p. 70–78, https://doi.org/10.1016/0012-821X(84)90039-6.

Valsami-Jones, E., and Ragnarsdottir, K.V., 1997, Controls on uranium and thorium behaviour in ocean-floor hydrothermal systems: Examples from the Pindos ophiolite, Greece: Chemical Geology, v. 135, no. 3–4, p. 263–274, https://doi.org/10.1016/S0009-2541(96)00121-0.

Vermeesch, P., 2018, IsoplotR: A free and open toolbox for geochronology: Geoscience Frontiers, v. 9, no. 5, p. 1479–1493, https://doi.org/10.1016/j.gsf.2018.04.001.

Wafforn, S., Seman, S., Kyle, J.R., Stockli, D., Leys, C., Sonbait, D., and Cloos, M., 2018, Andradite garnet U-Pb geochronology of the big Gossan skarn, Ertsberg-Grasberg mining district, Indonesia: Economic Geology and the Bulletin of the Society of Economic Geologists, v. 113, no. 3, p. 769–778, https://doi.org/10.5382/econgeo.2018.4569.

Wang, B., Hu, X., Wang, J., Shao, Q., Ling, J., Guo, N., Zhao, Y., Xia, Z., and Jiang, C., 2011, Geological characteristics and genesis of Chagangnuoer iron deposit in western Tianshan, Xinjiang: Mineralium Deposita, v. 30, no. 3, p. 385–402.

Wang, B., Shu, L., Liu, H., Gong, H., Ma, Y., Mu, L., and Zhong, L., 2014, First evidence for ca. 780 Ma intraplate magmatism and its implications for Neoproterozoic rifting of the North Yili block and tectonic origin of the continental blocks in SW Central Asia: Precambrian Research, v. 254, p. 258–272, https://doi.org/10.1016/j.precamres.2014.09.005.

Wang, F.Y., Ge, C., Ning, S.Y., Nie, L.Q., Zhong, G.X., and Noel, C.W., 2017, A new approach to LA-ICP-MS mapping and application in geology: Acta Petrologica Sinica (Yanshi Xuebao), v. 33, no. 11, p. 3422–3436.

Wang, Y.L., Li, Z.Y., and Wang, Y., 2007, Geological characteristics of iron deposits in Fanchang area, Anhui Province, East China: Express Information of Mining Industry, v. 462, p. 75–77.

Whitney, D.L., and Evans, B.W., 2010, Abbreviations for names of rock-forming minerals: The American Mineralogist, v. 95, no. 1, p. 185–187, https://doi.org/10.2138/am.2010.3371.

Whitney, P.R., and Olmsted, J.F., 1998, Rare earth element metasomatism in hydrothermal systems: The Willsboro-Lewis wollastonite ores, New York, USA: Geochimica et Cosmochimica Acta, v. 62, no. 17, p. 2965–2977, https://doi.org/10.1016/S0016-7037(98)00230-0.

Woodhead, J.D., and Hergt, J.M., 2010, Strontium, neodymium and lead isotope analyses of NIST glass certified reference materials: SRM 610, 612, 614: Geostandards and Geoanalytical Research, v. 25, no. 2–3, p. 261–266.

Xiao, X., Zhou, T.-f., White, N.C., Zhang, L.-j., Fan, Y., Wang, F.-y., and Chen, X.-f., 2018, The formation and trace elements of garnet in the skarn zone from the Xinqiao Cu-S-Fe-Au deposit, Tongling ore district, Anhui Province, eastern China: Lithos, v. 302–303, p. 467–479, https://doi.org/10.1016/j.lithos.2018.01.023.

Xu, G., and Lin, X., 2000, Geology and geochemistry of the Changlongshan skarn iron deposit, Anhui Province, China: Ore Geology Reviews, v. 16, no. 1–2, p. 91–106, https://doi.org/10.1016/S0169-1368(99)00025-6.

Xu, J., Ciobanu, C.L., Cook, N.J., Zheng, Y., Sun, X., and Wade, B.P., 2016, Skarn formation and trace elements in garnet and associated minerals from Zhibula copper deposit, Gangdese belt, southern Tibet: Lithos, v. 262, p. 213–231, https://doi.org/10.1016/j.lithos.2016.07.010.

Yan, S., Shan, Q., Niu, H.-C., Yang, W.-B., Li, N.-B., Zeng, L.-J., and Jiang, Y.-H., 2015, Petrology and geochemistry of late Carboniferous hornblende gabbro from the Awulale Mountains, western Tianshan (NW China): Implication for an arc–nascent back-arc environment: Journal of Asian Earth Sciences, v. 113, no. 1, p. 218–237, https://doi.org/10.1016/j.jseaes.2015.01.016.

Yan, S., Niu, H.-C., Zhao, J.-x., Bao, Z.-W., and Sun, W.-d., 2018, Ore-fluid geochemistry and metallogeny of the Dunde iron-zinc deposit in western Tianshan, Xinjiang, China: Evidence from fluid inclusions, REE and C-O-Sr isotopes of calcite: Ore Geology Reviews, v. 100, p. 441–456, https://doi.org/10.1016/j.oregeorev.2016.06.024.

Yang, F., Geng, X., Li, Q., and Chai, F., 2016, Iron Polymetallic Deposits in Northern Xinjiang: Beijing, Geological Publishing House, 408 p.

Yang, Y.H., Wu, F.Y., Yang, J.H., Mitchell, R.H., Zhao, Z.F., Xie, L.W., Huang, C., Ma, Q., Yang, M., and Zhao, H., 2018, U-Pb age determination of schorlomite garnet by laser ablation inductively coupled plasma mass spectrometry: Journal of Analytical Atomic Spectrometry, v. 33, p. 231–239, https://doi.org/10.1039/C7JA00315C.

Zhang, X., Tian, J.Q., Gao, J., Klemd, R., Dong, L.H., Fan, J.J., Jiang, T., Hu, C.J., and Qian, Q., 2012a, Geochronology and geochemistry of granitoid rocks from the Zhibo syngenetic volcanogenic iron ore deposit in the western Tianshan Mountains (NW-China): Constraints on the age of mineralization and tectonic setting: Gondwana Research, v. 22, p. 585–596, https://doi.org/10.1016/j.gr.2011.06.007.

Zhang, X., Klemd, R., Gao, J., Dong, L.-H., Wang, X.-S., Haase, K., Jiang, T., and Qian, Q., 2015, Metallogenesis of the Zhibo and Chagangnuoer volcanic iron oxide deposits in the Awulale iron metallogenic belt, western Tianshan orogen, China: Journal of Asian Earth Sciences, v. 13, no. 1, p. 151–172.

Zhang, Z., Hong, W., Jiang, Z., Duan, S., Xu, L., Li, F., Guo, X., and Zhao, Z., 2012b, Geological characteristics and zircon U-Pb dating of volcanic rocks from the Beizhan iron deposit in western Tianshan Mountains, Xinjiang, NW China: Acta Geologica Sinica–English Edition, v. 86, no. 3, p. 737–747, https://doi.org/10.1111/j.1755-6724.2012.00699.x.

Zhang, Z., Hou, T., Santosh, M., Li, H., Li, J., Zhang, Z., Song, X., and Wang, M., 2014, Spatio-temporal distribution and tectonic settings of the major iron deposits in China: An overview: Ore Geology Reviews, v. 57, p. 247–263, https://doi.org/10.1016/j.oregeorev.2013.08.021.

Zheng, Y., Huang, W.-h., Zhou, Y., Zhao, Z.-g., Xin-cheng, G., and Chen, Z.-h., 2014, Geochemistry, geochronology and geological implication of intrusive rock from Beizhan iron deposit of Xinjiang: Journal of Earth Sciences and Environment, v. 36, no. 2, p. 38–50.